

# Effects of Redshift Uncertainty on Cross-Correlations of CMB Lensing and Galaxy Surveys

Ross Cawthon\*

*Department of Astronomy and Astrophysics, The University of Chicago, 5640 S. Ellis Ave, Chicago, IL, 60637, USA*

*Kavli Institute for Cosmological Physics, The University of Chicago, Chicago, IL, 60637, USA*

(Dated: May 18, 2022)

We explore the effects of incorporating redshift uncertainty into measurements of galaxy clustering and cross-correlations of galaxy positions and CMB lensing maps. We use a simple Gaussian model for a redshift distribution in a redshift bin with two parameters, the mean,  $z_0$ , and the width,  $\sigma_z$ . We vary these parameters, as well as the galaxy bias,  $b_g(z)$ , and cosmological parameters  $\sigma_8(z)$  and  $\Omega_m$  in a Fisher analysis across 12 redshift bins from  $z = 0 - 7$ . We find that incorporating redshift uncertainties degrades constraints on cosmological parameters in the LSST/CMB-S4 era by about a factor of 10 compared to the case of perfect redshift knowledge. In our fiducial analysis of LSST/CMB-S4 including redshift uncertainties, we project constraints on  $\sigma_8(z)$  for  $z < 3$  of less than 5%. Galaxy imaging surveys are expected to have priors on redshift parameters from photometric redshift algorithms and other methods. When adding priors with the expected precision for LSST redshift algorithms, the constraints on  $\sigma_8(z)$  can be improved by a factor of 2-3 compared to the case of no priors. We also find that ‘self-calibrated’ constraints on the redshift parameters from just the auto-correlation and cross-correlation measurements (with no priors) are competitive with photometric redshift techniques. In the LSST/CMB-S4 era, we find uncertainty on the redshift parameters ( $z_0, \sigma_z$ ) to be below  $0.004(1+z)$  at  $z < 1$ . For all parameters, constraints improve significantly if smaller scales can be used. We also project constraints for nearer term survey combinations: DES/SPT-SZ, DES/SPT-3G and LSST/SPT-3G.

## I. INTRODUCTION

Large galaxy imaging surveys provide a wealth of cosmological information about the Universe. In particular, these surveys can probe the growth of structure across cosmic time. Such measurements can distinguish between different models for the mechanism causing cosmic acceleration [1]. Two specific probes used by galaxy surveys to study structure growth are galaxy clustering and weak gravitational lensing. Recent and ongoing imaging surveys using these probes include the Dark Energy Survey (DES, [2]), the Kilo-Degree Survey (KIDS, [3]), the Canada-France-Hawaii Telescope Lensing Survey (CFHTLenS, [4]) and the Hyper-Suprime Cam survey (HSC, [5]). The Dark Energy Survey recently produced the most comprehensive study of the growth of structure from an imaging survey [6] using galaxy clustering and weak lensing measurements from its first year of data ([7], [8], [9]). The DES Data Release 1 includes more than 300 million galaxies from the first three years of data [10]. In the next decade, the constraining power of imaging surveys will increase greatly when the Large Synoptic Survey Telescope (LSST, [11]) begins operations. It is expected to find on the order of several billion galaxies [12]. LSST will also greatly extend the redshift coverage of imaging surveys.

A special case of using gravitational lensing to infer the structure of matter in the Universe is lensing of the cosmic microwave background (CMB). The CMB is made up of photons that have been free streaming since redshift  $z \approx 1100$  (see e.g., [13]). CMB lensing thus measures lensing from matter over nearly the entire lifetime of the Universe, more than 13 billion years. The first detection of CMB lensing was found by doing a cross-correlation of radio galaxies from

the NRAO VLA Sky Survey (NVSS) and CMB data from the Wilkinson Microwave Anisotropy Probe (WMAP) [14]. CMB lensing has since been detected in a number of ways including CMB only methods and cross-correlations with several tracers of large-scale structure, including the cosmic infrared background (CIB), quasars, clusters and galaxies detected in a number of different wavelengths (see [15] for an extensive list).

The cross-correlation of galaxy positions and CMB lensing is a particularly useful measurement of cosmic structure. While CMB lensing maps are impacted by matter back to  $z \approx 1100$ , they have the disadvantage of having no way to distinguish the redshifts of the matter lensing any particular location in the sky. All the information back to  $z \approx 1100$  is stacked into one two-dimensional projection. Galaxies, having redshift measurements, provide a three-dimensional estimate of a location of matter. However, galaxy clustering alone suffers from the fact that galaxies do not directly trace the total underlying distribution of matter in the Universe, but instead are biased tracers. In galaxy clustering measurements, this galaxy bias (the relationship between the distribution of galaxies and total matter) is degenerate with the overall clumpiness of the Universe (i.e.  $\sigma_8$ ) which provides information on competing cosmological models. The cross-correlation of galaxies and CMB lensing provides both a measurement of matter as a function of redshift, and a way to break the degeneracy of galaxy bias and matter clumpiness. The cross-correlation also has the advantage of having very different systematic effects present. Galaxy surveys (of usually optical or infrared light) and CMB experiments (in the microwave band) operate in a number of different ways, making correlated systematic effects in both surveys unlikely.

These cross-correlations of galaxy clustering and CMB lensing have been measured by a number of recent experiments (see [16] for a recent list). In particular, [15] cross-correlated CMB lensing maps from both the South Pole Tele-

\* Now at Department of Physics, University of Wisconsin-Madison, 1150 University Ave, Madison, WI, 53706, USA.; cawthon@wisc.edu

scope (SPT) [17] and the Planck Satellite [13] with Dark Energy Survey galaxies from  $z = 0.2 - 1.2$ . Among current measurements, this analysis using a large optical cosmic survey out to high redshifts ( $z > 1$ ) most closely mimics the type of measurements we will address in this work. Recently a projection of the constraining power of a future measurement using LSST and the planned experiment, CMB-S4 [18] was made by [19]. However, a critical element that many of these studies do not incorporate in detail are the effects of redshift uncertainties on these measurements (though [52] and [19] briefly explore the issue).

While there are spectroscopic galaxy surveys (e.g., BOSS, [20] and in the future, DESI [21]), many of the best cosmological constraints (e.g., DES [6]) from galaxy clustering and gravitational lensing come from larger, deeper imaging surveys which suffer the downside of having only photometric redshifts from color bands. Much work goes into training these photometric redshift codes to be as accurate as possible by using spectroscopic training sets of galaxies (e.g., [22], [23] and references therein). The method of spatially cross-correlating photometric galaxies with smaller samples of spectroscopic galaxies to infer redshift distributions (also known as ‘clustering redshifts’) has also seen success (e.g., [24], [25], [26], [27] and references therein). However, even future photometric surveys like LSST expect significant uncertainty in their redshift distributions due to photometric redshift errors. Since LSST will probe higher redshifts than current surveys like the Dark Energy Survey, the issues surrounding photometric redshifts are likely to be compounded. Both the typical photometric training methods and the clustering method need spectroscopic galaxies at the same redshifts probed by the photometric survey. The photometric methods also need spectroscopic samples of galaxies with similar magnitude depth for training. Both getting the necessary number of spectroscopic measurements of galaxy redshifts and insuring that current methods are sufficiently accurate at higher redshifts will be significant challenges.

Another interesting method to infer redshifts that has emerged is the idea of ‘self-calibrating’ the redshift measurements from cosmological correlation functions themselves (e.g., galaxy clustering, weak lensing measurements etc.) Work by [28] recently explored this idea with several types of correlation functions while holding cosmology fixed. Such methods may be needed in the future to supplement the current methods of photometric redshift calibration.

In this work, we project the constraints from measurements of galaxy clustering and cross-correlations between galaxy positions and CMB lensing for current and future surveys. We use a Fisher analysis similar to [19]. Unlike previous work though, we include redshift parameters in the Fisher analysis.<sup>1</sup>

There are two main objectives of this work: 1. To as-

sess how redshift uncertainties affect the expected cosmological constraints from galaxy survey and CMB lensing cross-correlations (i.e. an extension of [19]) and 2. To assess how well the self-calibrating approach can constrain redshift distributions when cosmological parameters are allowed to vary (i.e. an extension of [28]).

We focus on the cross-correlation of galaxy clustering and CMB lensing to more directly explore these two goals, though we note similar questions could be asked when including optical weak gravitational lensing data which can also be cross-correlated with CMB lensing (see e.g., [29], [30]). For cosmological constraints, we focus on  $\sigma_8$  as the main parameter that can be studied with these probes. Focusing on this parameter allows us to study carefully the impact of redshift uncertainties.

The setup of this paper is as follows: In Section II, we discuss the datasets used in this paper and their projected parameters. In Section III, we discuss how we model and parameterize redshift distributions when accounting for photometric redshift errors. In Section IV, we outline the projected power spectra measurements used in this work, and the Fisher Matrix formalism we use to project constraints on cosmological and redshift parameters. In Section V, we show Fisher constraints from an analysis without redshift uncertainties. In Section VI, we show our fiducial Fisher analysis incorporating redshift uncertainties. In Section VII, we explore in more detail how our constraints depend on various survey parameters, including priors on the redshift parameters. In Section VIII, we explore in more detail how successful our analysis is in constraining the redshift parameters. In Section IX, we give our conclusions.

## II. DATASETS

### A. Dark Energy Survey (DES)

The Dark Energy Survey is an ongoing 5-year photometric survey covering  $5,000 \text{ deg}^2$  in the  $g, r, i, z, y$  bands [2]. DES observes from the Blanco Telescope at the Cerro Tololo Inter-American Observatory (CTIO) in Chile. We assume a galaxy distribution for DES from [31] which gives:

$$n(z) \propto (z/z_*)^\alpha \exp[-(z/z_*)^\beta] \quad (1)$$

where for DES the parameters are  $\alpha = 1.25, \beta = 2.29$  and  $z_* = 0.88$  with the total number of galaxies having a density of  $12 \text{ arcmin}^{-2}$ . This redshift distribution is shown in Figure 1. The full DES will cover  $5,000 \text{ deg}^2$ , however SPT only covers  $2,500 \text{ deg}^2$ , making the observed fraction of the sky  $f_{\text{sky}} = 0.0606$  for the projected power spectra.

### B. Large Synoptic Survey Telescope (LSST)

The Large Synoptic Survey Telescope is a 10-year photometric survey based at Cerro Pachón in Chile. It is expected

<sup>1</sup> We note that [19] does use redshift parameters in part of its analysis (Section VIII). They specifically model catastrophic redshift outliers though, not the generic Gaussian-like photometric redshift errors which our work will focus on.

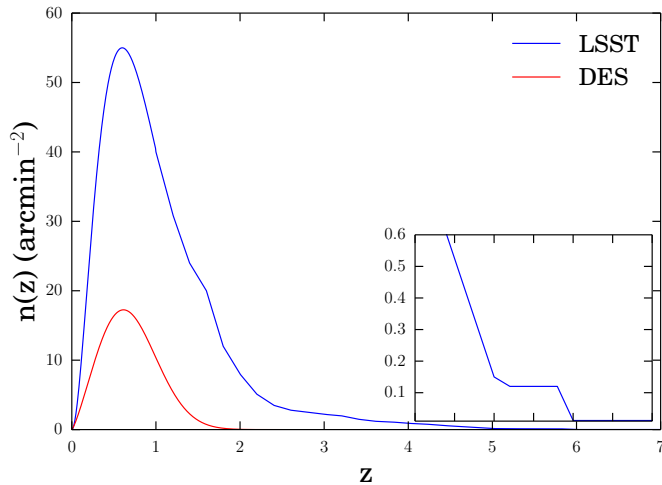


FIG. 1. The expected galaxy redshift distributions from DES and LSST used in this work. The redshift distributions come from [31] for DES and [19] for LSST. The inset shows  $4 < z < 7$ .

to start main operations in 2022. Its main deep-fast-wide survey will cover  $18,000 \text{ deg}^2$  ( $f_{\text{sky}} = 0.45$ ) [12]. However, for our fiducial analysis we will use  $f_{\text{sky}} = 0.5$  to more easily compare with the results in [19]. For the galaxy distribution in LSST, we match to the prediction used in [19] (Figure 4) for galaxies with  $i$ -magnitude  $< 27$  after 3 years of data, shown in our Figure 1. The prediction comes from LSST simulations in [32] for  $0 < z < 4$ . We note that for  $z < 1$ , this  $n(z)$  matches closely the LSST power law prediction from [31]. [19] also add galaxies for  $4 < z < 7$  by extrapolating from recent results from the Subaru Hyper-Suprime Cam GOLDRUSH program [33] which found more than half a million candidates for  $4 < z < 7$  galaxies based on the dropout technique [34].

### C. South Pole Telescope SZ Survey (SPT-SZ)

The South Pole Telescope (SPT) is a 10-meter millimeter wave, wide-field telescope at the Amundsen-Scott South Pole station in Antarctica [17]. The  $2,500 \text{ deg}^2$  SPT-SZ survey is described in [35]. A CMB lensing map from this survey was made in [36]. More recently, [37] made a map covering the full survey, while also including data from the Planck Satellite [38]. The lensing maps are made using the quadratic estimator technique [39]. The lensing maps from SPT-SZ are made from measurements in the 150 GHz band. In this band, the temperature maps have a typical noise of  $\Delta_T = 18 \mu\text{K arcmin}$ . For the expected CMB lensing noise in the auto-power spectrum (i.e.  $N_l^{KK}$ ), we use the noise measurement in [15] which used a version of the maps made in [36]. The measured lensing noise of the maps in [37] are very similar. The lensing noise for SPT-SZ as well as the projected noise for the following two experiments, SPT-3G and CMB-S4, are shown in Figure 2

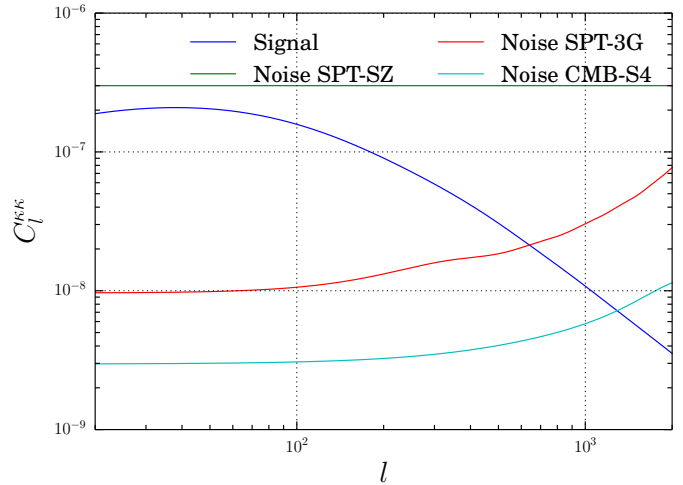


FIG. 2. The CMB lensing noise for the experiments we consider, as well as the signal of the CMB lensing auto power spectrum,  $C_l^{KK}$ . We use SPT noise estimates from [15] and the CMB-S4 estimate from [19]. These noise estimates enter our analysis in Equation 8.

### D. South Pole Telescope 3G Survey (SPT-3G)

The SPT-3G survey [40] is the third generation survey on the South Pole Telescope, following the SPT-SZ survey, and the SPT-Pol survey [41]. We will not discuss the SPT-Pol survey due to its smaller sky coverage than SPT-SZ or SPT-3G. SPT-3G has an improved optical design allowing for more pixels in the optical plane, and uses multi-choric pixels as described in [40]. These improvements should lower the temperature noise by roughly a factor of ten compared to SPT-SZ. Like SPT-Pol, SPT-3G will also have polarization measurements. It will cover the full  $2,500 \text{ deg}^2$  which was observed by SPT-SZ. For the projection of SPT-3G noise, we use an estimate by the South Pole Telescope team using a minimum-variance estimator, which is shown in [15]. We show this projected noise in Figure 2.

### E. CMB-S4

The CMB-S4 experiment [42] is a next generation CMB survey expected to begin within the next decade. It is likely to have operations in both Antarctica and Chile. The sky coverage is still uncertain, though many projections have CMB-S4 covering half the sky, overlapping completely LSST. We will assume this for our fiducial analysis, giving  $f_{\text{sky}} = 0.5$ . For the CMB lensing noise, we use the estimate in [19] and show this in Figure 2. This estimate assumes  $\Delta_T = 1 \mu\text{K arcmin}$  noise and a minimum variance combination of multiple lensing estimators from the T, E and B mode measurements of a CMB experiment [42].

### III. PARAMETERIZING REDSHIFT DISTRIBUTIONS

A focus of this work is to study the effects of redshift uncertainty on cosmological projections using galaxy and CMB lensing surveys. With this in mind, the observed galaxy distributions in a photometric survey like DES or LSST will never quite look like the redshift distributions mentioned in Section II. In a typical photometric survey, galaxies are binned by photometric redshift. High-density, faint samples of galaxies (such as the predicted distribution of  $i < 27$  galaxies in LSST in Figure 1) typically have photometric redshift errors consistent with a Gaussian scatter. For example, LSST predicts photometric redshifts with a scatter of  $\sigma_{\text{ph}} = 0.05(1+z)$  around the true redshift ([43], [12]).

To simulate what a photometrically selected and binned redshift distribution looks like, we first take the expected  $n(z)$  from the references in Section II. We then draw galaxies from this distribution and assign them photometric redshifts, assuming the photometric redshift errors follow  $\sigma_{\text{ph}} = 0.05(1+z)$ , with no bias (i.e.  $\bar{z}_{\text{true}} = \bar{z}_{\text{ph}}$ ). We then simulate what would be done for a real survey and bin the galaxies by  $z_{\text{ph}}$ . As can be seen in Figure 3, the true redshift distribution (the sum of  $z_{\text{true}}$ , not the sum of  $z_{\text{ph}}$ ) after binning by photometric redshifts is nearly Gaussian in shape. To further show this, in Figure 3 we also plot a Gaussian with the mean redshift and standard deviation of the redshifts in the binned  $n(z)$ . We emphasize that Figure 3 shows only true redshift distributions, and does not mimic what a photometric redshift code would predict, as can be seen that, e.g., the  $n(z)$  goes beyond the borders of the redshift bin,  $z = 1.0$  and  $z = 1.5$  (the Gaussian on the right of the Figure).

In current surveys, photometric binning often produces Gaussian-like true redshift distributions in each bin (e.g., [6]) similar to Figure 3. These true redshift distributions are verified to some degree by testing photometric redshift codes on samples of galaxies with spectroscopic redshifts (e.g., [22]) or using other methods like the cross-correlations of photometric and spectroscopic galaxies to recover the redshift distribution of the photometric set (e.g., [25], [26]). However, each of these methods has uncertainties. Exact knowledge of the redshift distribution for a photometric survey is unlikely.

Given the typical case of a Gaussian-like true redshift distribution when binning by photometric redshifts, we parameterize the redshift distributions in our main analysis (Section VI) with Gaussians of mean  $z_0$  and width  $\sigma_z$ . This makes the redshift distribution in a bin,  $i$ :

$$n(z)_i \propto \frac{1}{\sigma_{z,i}} \exp\left[-\frac{(z - z_{0,i})^2}{2\sigma_{z,i}^2}\right]. \quad (2)$$

For our fiducial analysis beginning in Section VI, we use 12 tomographic redshift bins with a Gaussian redshift distribution in each bin. These redshift distributions are shown in Figure 4, along with the full  $n(z)$  prediction for LSST from [19]. We also show the CMB lensing kernel (described in Equation 4) which shows what redshifts most efficiently lens the CMB. The lensing kernel peaks at about  $z \approx 2$ . In Section VI and later, we allow the parameters  $z_{0,i}$  and  $\sigma_{z,i}$  of each

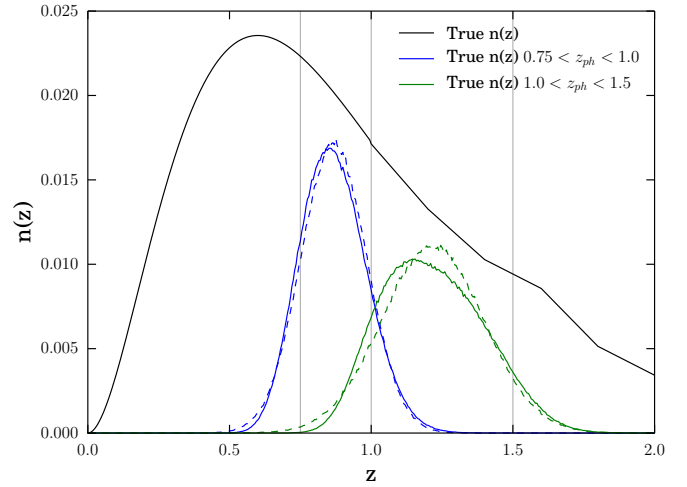


FIG. 3. The true redshift distribution and examples of photometric redshift bins we use. Shown in black is the true  $n(z)$  for LSST, though it actually extends out to  $z = 7$ . In blue and green are examples of the  $n(z)$  in photometrically-selected redshift bins. As seen, e.g., a bin with photometric cutoffs of  $z = 0.75$  and  $z = 1.0$  (blue) will have its true distribution extend beyond those boundaries (lined in gray). The modeled true distributions of the binned galaxies are close to being Gaussians. The dotted lines show Gaussians with the same mean and standard deviation of the true binned distributions.

of the Gaussians in Figure 4 to vary in our Fisher analysis (Section IV B). This gives a simple framework for accounting for redshift uncertainties in the Fisher analysis and should be accurate in the limit that the binned redshift distributions are Gaussian.

## IV. METHODS

### A. Power Spectra

The CMB lensing convergence,  $\kappa$ , in a given line of sight,  $\hat{n}$ , is the integral over all the matter fluctuations that will cause gravitational lensing:

$$\kappa(\hat{n}) = \int dz W^\kappa(z) \delta(\chi(z)\hat{n}, z), \quad (3)$$

where  $\delta(\chi(z)\hat{n}, z)$  is the overdensity of matter at comoving distance,  $\chi$  and redshift,  $z$ . The distance kernel,  $W^\kappa$ , is given by

$$W^\kappa(z) = \frac{3}{2} \Omega_m H_0^2 \frac{(1+z)}{H(z)} \frac{\chi(z)}{c} \left[ \frac{\chi(z_{\text{cmb}}) - \chi(z)}{\chi(z_{\text{cmb}})} \right] \quad (4)$$

where  $\Omega_m$  is the fraction of the matter density today compared to the present critical density of the Universe,  $H_0$  is the Hubble parameter today,  $H(z)$  is the Hubble parameter as a function of redshift,  $c$  is the speed of light and  $\chi_{\text{cmb}}$  is the comov-

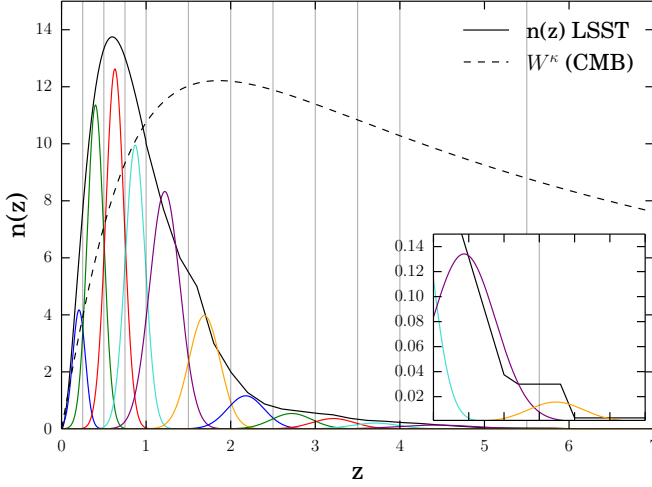


FIG. 4. The 12 Gaussian redshift distributions for our tomographic redshift bins which will be used in our analysis starting in Section VI. Also shown is the full  $n(z)$  prediction for LSST from which the Gaussian distributions are estimated in the manner described in Section III and Figure 3. We also show  $W^\kappa$  from Equation 4, which is the CMB lensing kernel. This parameter weights the redshifts that most efficiently lens the CMB. The curve for  $W^\kappa$  is normalized to the full  $n(z)$  curve.

ing distance to the surface of last scattering where the CMB was emitted [44].

As galaxies are expected to be biased tracers of matter fluctuations, the galaxy overdensity in a given line of sight is

$$g(\hat{n}) = \int dz W^g(z) b_g(z) \delta(\chi(z) \hat{n}, z), \quad (5)$$

where  $b_g(z)$  is the galaxy bias, the ratio of the overdensity of galaxies to the overdensity of matter, assumed here to be independent of scale, and the kernel  $W^g$  is given by

$$W^g(z) = \frac{1}{n_{\text{tot}}} \frac{dn(z)}{dz} \quad (6)$$

where  $n_{\text{tot}}$  is the total number of galaxies in the sample and  $\frac{dn(z)}{dz}$  is the redshift distribution of those galaxies.

At small angular scales, we can use the Limber approximation ([45], [46]) to write the cross power spectrum of two of our fields,  $i$  and  $j$ , where  $i, j \in \kappa_{\text{CMB}}, g_{z=0-0.25}, g_{z=0.25-0.5}, \dots$  at multipole  $l$  as

$$C_l^{ij} = \int \frac{dz}{c} \frac{H(z)}{\chi(z)^2} W^i(z) W^j(z) P(k = \frac{l}{\chi(z)}, z) \quad (7)$$

where  $P(k = \frac{l}{\chi(z)}, z)$  is the matter power spectrum at wavenumber  $k$  for a given redshift  $z$ . We calculate all of the power spectra using the Planck 2015 flat- $\Lambda$ CDM cosmological parameters including external data [47]. These parameters are  $h = 0.6774$ ,  $\Omega_m = 0.3089$ ,  $\Omega_b = 0.04860$ ,

$\tau = 0.066$ ,  $n_s = 0.9667$ ,  $A_s = 2.1413 \times 10^9$  at a pivot scale of  $k = 0.05 \text{ Mpc}^{-1}$ , corresponding to  $\sigma_{8,0} = 0.8159$ . The matter power spectrum,  $P(k, z)$ , is calculated using the Boltzmann code in the CAMB program ([48], [49]) with the program Halofit ([50]) to calculate the non-linear regime of clustering.

The Gaussian covariances for the power spectra,  $C_l$ , are:

$$\text{cov}(\hat{C}_l^{ij}, \hat{C}_l^{i'j'}) = \frac{\delta_{ll'}}{f_{\text{sky}}(2l+1)} + (\hat{C}_l^{ii'} \hat{C}_l^{jj'} + \hat{C}_l^{ij'} \hat{C}_l^{ji'}) \quad (8)$$

where the upper indices  $i$  and  $j$  again refer to the different fields. The power spectra denoted by  $\hat{C}$  include noise:

$$\hat{C}_l = C_l(\text{theory}) + N_l \quad (9)$$

where for galaxy auto-correlations, the shot noise term is  $N_l = 1/\rho$  where  $\rho$  is the galaxy density per steradian, and for the CMB lensing auto-correlation, the predicted  $N_l$  for different CMB experiments is shown in Figure 2. For cross-correlations,  $N_l = 0$ . Equation 8 ignores non-Gaussian corrections for CMB lensing and galaxy clustering covariance.

We show some sample power spectra in Figure 5 for two of the twelve redshift bins used in the fiducial analysis (Figure 4). Shown are galaxy auto-correlations, cross-correlations between galaxy bins, cross-correlations between galaxies and CMB lensing, and the CMB lensing auto-correlation. The error bands represent the covariance ( $\text{cov}(C_l^{ii}, C_l^{ii})$ ) estimates of the LSST/CMB-S4 era. Also shown are some of the relevant noise levels,  $N_l$ , for the different experiments. We can see that many more of the multipoles of the cross-correlation between galaxies and CMB lensing are signal dominated in the LSST/CMB-S4 era compared to the DES/SPT-SZ era.

## B. Fisher Matrix

We use a Fisher Matrix formalism similar to [19] (Section VI) to derive constraints on parameters. The Fisher formalism assumes all the cosmological information is contained in the power spectra, which is true in the limit that the fields are Gaussian. In our fiducial analysis (Section VI), we have 12 tomographic redshift bins of galaxies (Figure 4), and the CMB lensing field,  $\kappa$ . This gives us  $N = 13$  fields, which means there are 13 auto-spectra and  $N(N-1)/2 = 78$  cross-spectra, for a total of 91 spectra. However, we assume the cross-spectra of non-neighboring redshift bins are zero. This reduces the total number of non-zero spectra to  $3(N-1) = 36$ .

Following [19], we define a large one-dimensional vector containing all the spectra:

$$\mathbf{d} = (d_{l_{\min}}, d_{l_{\min}+1}, \dots, d_{l_{\max}}). \quad (10)$$

For each  $l$ ,

$$d_l = (C_l^{11}, C_l^{12}, \dots, C_l^{NN}) \quad (11)$$



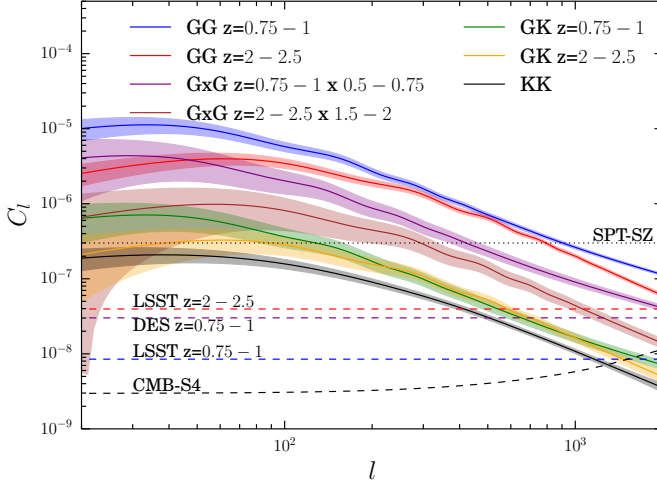


FIG. 5. Sample angular power spectra ( $C_l$ ) for different redshift bins (Figure 4) in our analysis. Shown are measurements for the bins with photometric redshifts between  $z = 0.75 - 1$  and  $z = 2 - 2.5$ . These measurements include galaxy auto-correlations (GG), cross-correlations between adjacent galaxy redshift bins (GxG) and cross-correlations of galaxies and CMB lensing (GK). Also shown is the CMB lensing auto-correlation (KK), the noise levels ( $N_l$ ) for the CMB experiments, SPT-SZ and CMB-S4, and the shot noise for the two galaxy bins in LSST and the  $z = 0.75 - 1$  bin in DES.

with  $N$  being the number of fields. Since  $C_l^{ij} = C_l^{ji}$ ,  $\mathbf{d}_l$  has  $N(N+1)/2$  spectra, 91 spectra when  $N = 13$  fields, with only 36 of these being non-zero as mentioned previously. The Fisher Matrix is then:

$$F_{ab} = \sum_{l=l_{\min}}^{l_{\max}} \frac{\partial \mathbf{d}_l}{\partial \theta_a} [\text{cov}(\mathbf{d}_l, \mathbf{d}_l)]^{-1} \frac{\partial \mathbf{d}_l}{\partial \theta_b} \quad (12)$$

where  $\theta$  is a parameter that depends on the measurements,  $\mathbf{d}_l$ , and  $a, b$  index the parameters. For our fiducial analysis, we use  $l_{\min} = 20$  and  $l_{\max} = 1000$  (similar to [19]), though we test other  $l_{\max}$  values. In all cases, we do not bin in  $l$  in this work. This Fisher setup assumes that the fields overlap (i.e. the CMB and galaxy experiments overlap completely on the sky), which is the case in the projected experiments of Section II. The projected error on a parameter,  $\theta$ , is then:

$$\sigma(\theta_a) \geq \sqrt{(F^{-1})_{aa}}. \quad (13)$$

In Section VII F, we analyze the effects of adding priors to our analysis. We add priors by substituting:

$$F_{aa} \rightarrow F_{aa} + \frac{1}{p(\theta_a)} \quad (14)$$

where  $p(\theta_a)$  is the prior on the parameter. When applying priors, Equation 14 is applied before the Fisher Matrix is inverted in Equation 13.

In our fiducial analysis, there are five types of parameters varied. These include the redshift parameters,  $z_{0,i}$  and  $\sigma_{z,i}$ , defined in Equation 2 for each of the redshift bins indexed by  $i$ . We also vary for each redshift bin,  $b_{g,i}$ , the galaxy bias and  $\sigma_{8,i}$ , which measures the amplitude of the matter power spectrum on scales of  $8 h^{-1}$  Mpc, where  $h = 100 \text{ km/sec/Mpc}/H_0$ . We use parameterizations similar to [19] for these latter two parameters. In Equation 5, we model the galaxy bias  $b_{g,i}$  as:

$$b_{g,i} = B_i(1+z). \quad (15)$$

While we will quote results on  $b_{g,i}$  through out this work, effectively the parameter being varied in the Fisher analysis is  $B_i$ . We implement  $\sigma_{8,i}$  into the power spectra (Equation 7) by substituting:

$$P(k, z) \rightarrow (1 + s_i)^2 P(k, z) \quad (16)$$

where  $s_i \equiv (\sigma_{8,i}/\sigma_{8,\text{fid}} - 1)$  is the fractional difference of  $\sigma_8$  in that bin compared to the fiducial cosmology. We note that when we calculate the CMB lensing auto-correlation,  $C_l^{\kappa\text{CMB}\kappa\text{CMB}}$  we apply  $s_i$  from the minimum and maximum photometric redshift boundaries for each bin  $i$ , though this does not map perfectly to the redshifts of the galaxies in bin  $i$ .<sup>2</sup>

The fifth type of parameter we allow to vary is the matter density of the Universe,  $\Omega_m$ . This parameter enters into  $P(k, z)$ , the calculation for  $H(z)$  as well as in the CMB lensing kernel,  $W^\kappa(z)$  (Equation 4). When we vary  $\Omega_m$ , we also vary  $\Omega_\Lambda$ , the cosmological constant energy density in  $\Lambda\text{CDM}$ , to keep the Universe flat.

The parameters  $z_{0,i}$ ,  $\sigma_{z,i}$ ,  $b_{g,i}$  and  $\sigma_{8,i}$  are measured in each redshift bin. Along with  $\Omega_m$ , this gives a total of  $n=4(N-1)+1$  parameters, which is 49 in the case of  $N=13$  fields. The Fisher matrix will be  $n \times n$  in size.

## V. RESULTS WITH NO REDSHIFT UNCERTAINTY

We first analyze the results of a Fisher matrix analysis when there is no redshift uncertainty. We briefly do an analysis that allows us to compare most directly to the results in [19]. We use the full  $n(z)$  of LSST (black line in Figure 4) and not the Gaussian redshift distributions as will be used in Section VI. We divide this  $n(z)$  into the 6 tomographic bins used in [19] with boundaries at  $z = [0, 0.5, 1, 2, 3, 4, 7]$ . Since there is no redshift uncertainty, here our Fisher setup has 6 values

<sup>2</sup> Since unlike [19], our redshift bins overlap, we must make a choice whether to tie the definition  $\sigma_{8,i}$  to a specific redshift range or to a specific redshift binned sample. We choose the latter as that is how many photometric redshift binned samples are analyzed (e.g., [15]). However, this does make how to specifically calculate  $\partial C_l^{\kappa\text{CMB}\kappa\text{CMB}} / \partial \sigma_{8,i}$  ill-defined since we are not defining  $\sigma_{8,i}$  to be a precise redshift range. In any case, the contributions of  $C_l^{\kappa\text{CMB}\kappa\text{CMB}}$  are very minor in the analysis, so we do not think this impacts the results significantly.

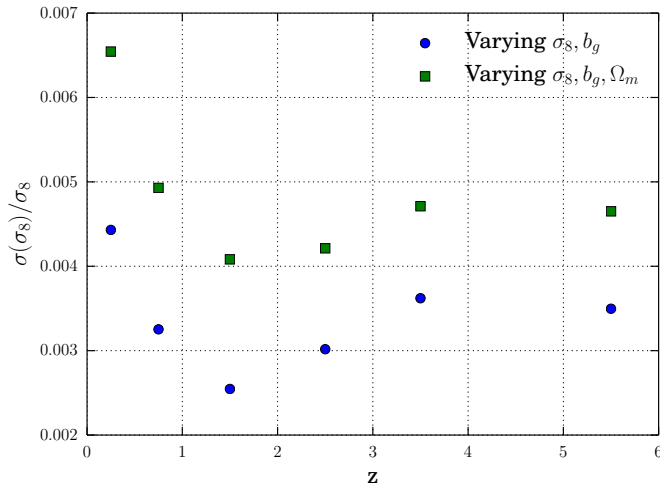


FIG. 6. The constraints on  $\sigma_8$  in the scenario with no redshift uncertainty for the LSST/CMB-S4 era. We plot both the case with  $\sigma_8$  and  $b_g$  allowed to vary in each bin (to be able to compare with the analysis in [19]) as well as the case with also  $\Omega_m$  being allowed to vary.

for  $\sigma_{8,i}$  and  $b_{g,i}$  and  $\Omega_m$  for 13 parameters. [19] does not vary  $\Omega_m$ , so we also show results without this parameter. We show the constraints on  $\sigma_8$  for this setup in Figure 6. We show how the results change as a function of  $l_{\max}$  in Figure 7. These constraints are nearly identical to [19] (Figure 9) when not including  $\Omega_m$  and about 30 – 60% larger when varying  $\Omega_m$ . The largest difference in our analysis here compared to [19] is that we do not include any SDSS or DESI galaxies at low redshifts as they do. This makes their constraints in the two lowest redshift bins better.

For our fiducial analysis in Section VI, we will use smaller redshift bins, splitting each of the bins used in [19] in half, giving us the 12 redshift bins shown in Figure 4. These smaller redshift bins are more similar to current analyses on data, such as from the Dark Energy Survey (e.g., [15], [6]). The approximation of a Gaussian redshift distribution as a result of photometric redshift binning (Section III) is also more accurate for smaller redshift bins. We first test the effect of the smaller bins while still having no redshift uncertainty. We divide the LSST  $n(z)$  distribution directly into twelve tomographic bins with boundaries at  $z = [0, 0.25, 0.5, 0.75, 1, 1.5, 2, 2.5, 3, 3.5, 4, 5.5, 7]$ . Again, we assume all redshifts can be known directly from the black line in Figure 4, and do not use the Gaussian distributions of that figure yet. In this setup, our Fisher analysis has 12 values for  $\sigma_{8,i}$  and  $b_{g,i}$  and  $\Omega_m$  for 25 parameters. The constraints on  $\sigma_8$  and  $b_g$  in this setup are shown in Figure 8. We again show the case with and without  $\Omega_m$  in the figures as well. Compared to Figure 6, the constraints on  $\sigma_8$  from doubling the number of redshift bins when not using  $\Omega_m$  are a little worse, as expected from shrinking the number of galaxies in each bin. The constraints are about 25 – 50% larger when comparing the average of two smaller bins with the larger bin

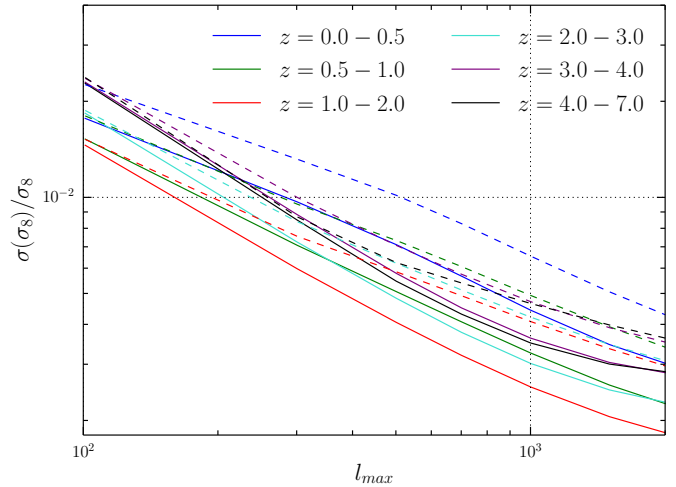


FIG. 7. Same analysis of  $\sigma_8$  constraints while having no redshift uncertainty as Figure 6, but with varying  $l_{\max}$  in the LSST/CMB-S4 era. This allows a direct comparison with the analysis of [19] (Figure 9). Our results are very similar. The dotted lines are for the case when we allow  $\Omega_m$  to vary as well, while the solid lines are with only varying  $\sigma_8$  and  $b_g$ .

of the same redshift range (e.g., comparing the average constraint between of  $z = 0 - 0.25$  and  $z = 0.25 - 0.5$  to the constraint on  $z = 0 - 0.5$ ). Of course, the benefit of more bins is gaining more precise information of the full  $\sigma_8(z)$ . Interestingly, when also varying  $\Omega_m$ , the constraints on  $\sigma_8$  have very little degradation when switching from 6 bins to 12 bins. With  $\Omega_m$  varying, the constraints on the smaller bins approximately equal the constraints on the larger bins (Figures 6 and 8). This is explained by the greater constraints on  $\Omega_m$  when increasing the number of bins (and thus, measurements to infer  $\Omega_m$ ). The constraints go from  $\sigma(\Omega_m) = 0.0007$  with 6 bins to  $\sigma(\Omega_m) = 0.0003$  with 12 bins.

## VI. RESULTS WITH REDSHIFT UNCERTAINTY

In this section, we show the fiducial analysis of varying five parameters in the Fisher analysis of Section IV B:  $\sigma_8(z), b_g(z), z_0(z), \sigma_z(z)$  in each redshift bin, and  $\Omega_m$ . With 12 redshift bins for our main analysis of an LSST-like sample, we have 49 parameters. The redshift distributions with central values of  $z_0(z)$  and Gaussian width  $\sigma_z(z)$  are shown in Figure 4.

For our fiducial analysis of the LSST/CMB-S4 era including redshift uncertainties, we show our constraints on the various parameters in Figures 9-10. Figure 9 shows the constraints on  $\sigma_8(z)$ , and  $b_g(z)$ , in the cases with and without redshift uncertainty (i.e. with  $z_0(z)$  and  $\sigma_z(z)$  fixed.)<sup>3</sup> We

<sup>3</sup> We note that the results for no redshift uncertainty in Figure 9 differ slightly

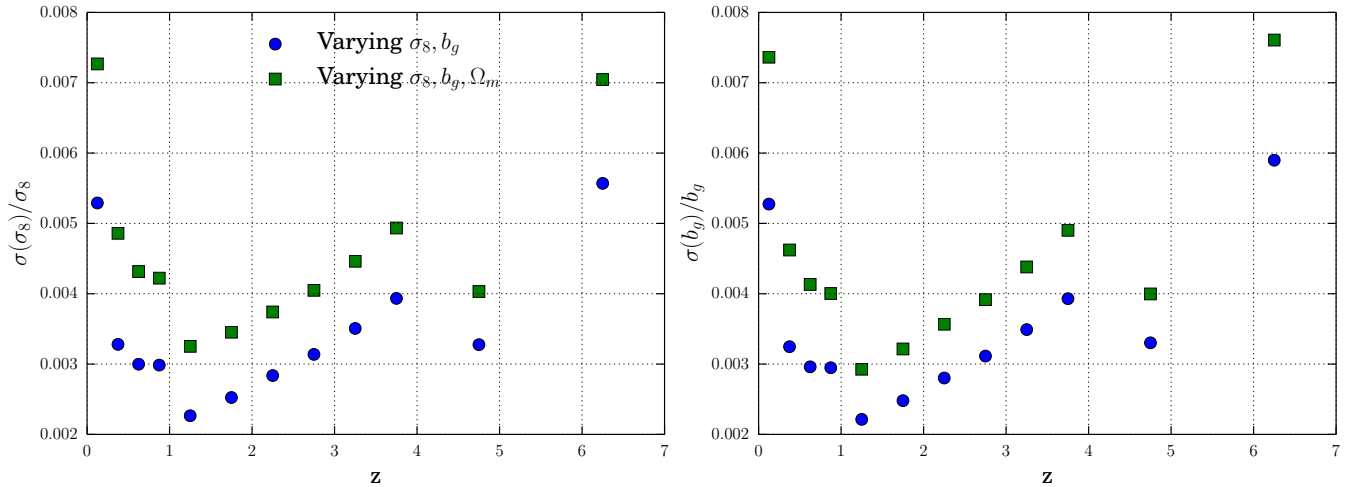


FIG. 8. Fractional constraints on  $\sigma_8$  and  $b_g$  as a function of redshift for the case of 12 tomographic redshift bins, and no redshift uncertainty. Plotted are the cases where  $\Omega_m$  is fixed or allowed to vary. The constraints largely weaken with higher redshift as the number density drops, however at  $z = 1.25$  and  $z = 4.75$ , the redshift width of the bin increases, leading to larger numbers of galaxies in the bin and smaller constraints.

can see that the addition of redshift uncertainty in these parameters increases errors on the other parameters by roughly a factor of ten. We also show the results for the parameters when cross-correlations of adjacent galaxy bins are not used (labeled as ‘no GxG’). In this case, errors on parameters tend to increase by another factor of two or more. This highlights the importance of the cross-correlations between galaxy bins, a measurement that in principle is not necessary when galaxy redshifts are known perfectly, and galaxy bins do not overlap in redshift space.

Figure 10 shows the constraints on the redshift parameters  $z_0$  and  $\sigma_z$  in each of the 12 photometric bins. We again also plot the results when not using the galaxy-galaxy cross-correlations of adjacent redshift bins. As seen in the figure, the galaxy-galaxy cross-correlations are of particular importance for  $\sigma_z$ . The cross-correlations break degeneracies between  $\sigma_8$ ,  $b_g$  and  $\sigma_z$  that remain when only having galaxy auto-correlations and galaxy-CMB lensing cross-correlations for each bin (see Appendix A for more discussion).

We also note that the constraints on  $\Omega_m$  in the scenarios of no galaxy-galaxy cross-correlations, the fiducial analysis, and the no redshift uncertainty case are  $\sigma(\Omega_m) = [0.00075, 0.00060, 0.00025]$  respectively. The improvement on  $\Omega_m$  with more redshift information is more mild than on  $\sigma_8$  due to  $\Omega_m$  not being part of the degeneracy of  $\sigma_8$ ,  $b_g$  and  $\sigma_z$  (Appendix A).

---

from Figure 8. This is due to the fact that the underlying galaxy distributions are slightly different in these two cases. In Figure 8, the underlying galaxy distribution is the true distribution binned by redshift (i.e. the black line in Figure 4 separated by the gray lines) similar to [19], while in Figure 9, the galaxy distribution in each bin is a Gaussian (colored lines in Figure 4) with parameters known exactly in the no redshift uncertainty case.

## VII. DEPENDENCE ON SURVEY PARAMETERS

### A. Example: DES-SPT

In this section, we vary different survey parameters that affect the precision of the constraints on the five types of parameters. We first look at a specific example of varying the survey parameters, using the expected galaxy density and redshift distributions from the full Dark Energy Survey, and CMB lensing noise from SPT-SZ and the future SPT-3G. This represents a nearer term projection for parameters using our methodology compared to the fiducial analysis of LSST/CMB-S4.

Figure 11 shows the constraints for the four parameters that exist in each redshift bin for DES+SPT-SZ, LSST+SPT-3G and our fiducial analysis on LSST+CMB-S4. Not shown are the constraints for the combination of DES+SPT-3g. These constraints are within 5% of the constraints for LSST+SPT-3G, in the bins where DES has data (the first 5 data points, up to  $z < 1.5$ ), so we do not show them. While the DES/SPT-SZ constraints are approximately factors of 2-3 weaker than LSST/CMB-S4, a  $\approx 10\%$  constraint on  $\sigma_8$  is still possible in all of our bins, and should be achievable with these surveys in the next few years. We show the constraints on  $\Omega_m$  for the different era analyses in Figure 12. We see that the constraints on  $\Omega_m$  improve by a factor of about 3-5 from the SPT/SZ era to the LSST/CMB-S4 era depending on the  $l_{\max}$  used. We also see that all eras of measuring the power spectra used in this work should improve upon the constraints from the recent DES year 1 analysis of galaxy clustering and weak lensing plus other data sets in [6].



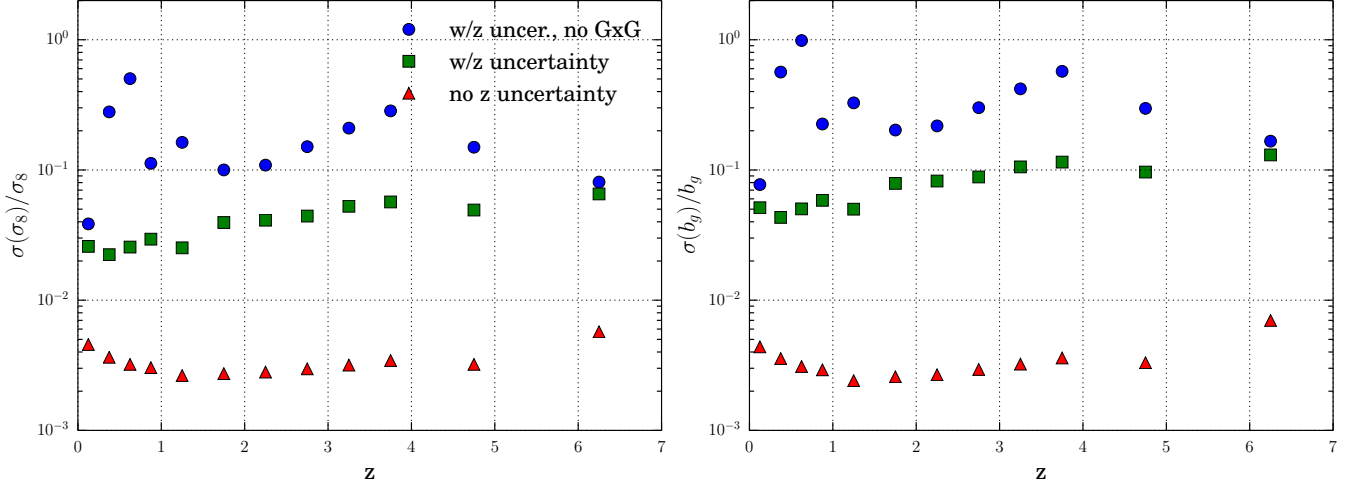


FIG. 9. Fractional constraints on  $\sigma_8$  and  $b_g$  for the fiducial case of LSST+CMB-S4, with  $l_{\max} = 1000$ , and  $f_{\text{sky}} = 0.5$ . Shown are the results with no redshift uncertainty, varying  $b_{g,i}$ ,  $\sigma_{8,i}$  for each redshift bin, as well as  $\Omega_m$ . Also shown is the fiducial analysis where we include redshift uncertainty by allowing the parameters  $z_{0,i}$  and  $\sigma_{z,i}$  to vary in each bin. We also show the case where we have redshift uncertainties, but do not use the cross-correlations of two adjacent galaxy bins in redshift space ('no GxG').

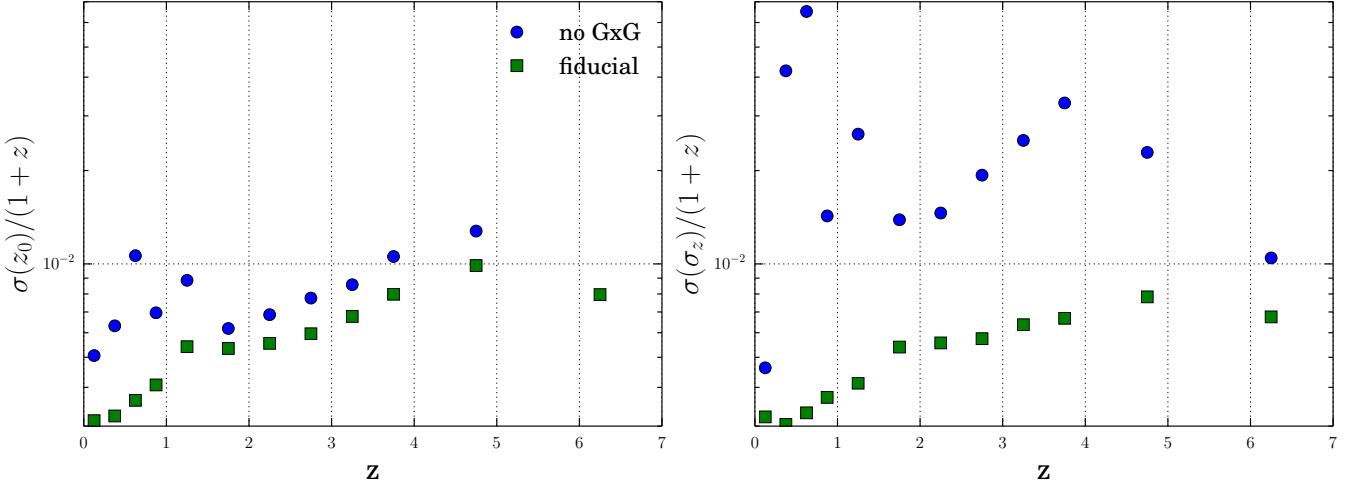


FIG. 10. The constraints on the mean redshift,  $z_0$ , and the width of the redshift distribution,  $\sigma_z$ , in each redshift bin for our fiducial analysis of Figure 9. We also show the constraints when the cross-correlations of two adjacent galaxy bins in redshift space are not used ('no GxG').

### B. Dependence on $l_{\max}$

The largest multipole,  $l_{\max}$  (smallest scale), to which these measurements can be used and modeled is a parameter with still a fair bit of uncertainty. In [15],  $l_{\max} = 2000$  was used for correlations of DES science verification data and SPT-SZ. However, in [51], they realize that a newer version (and perhaps older versions) of the SPT lensing map are significantly impacted by TSZ bias. This leads them to only use real space angular separations of  $15'$  or greater, roughly equivalent to using an  $l_{\max} = 720$ . In [19], they use  $l_{\max} = 1000$  for their fiducial projections, but also vary  $l_{\max}$  out to 2000. They cite

the issues of modeling non-linear galaxy bias at small scales (large  $l$ ) as a concern. [52] also looks extensively at the effects of modeling small scale non-linear bias on galaxy-CMB lensing cross-correlations. On the other hand, [15] and [53] find for DES science verification galaxies that linear galaxy bias is a good approximation in most cases down to  $l_{\max} = 2000$ , even though this can be a factor of 4 smaller than where the matter power spectrum becomes non-linear.

We chose  $l_{\max} = 1000$  for our fiducial analysis, but vary it in this section, much like the treatment in [19]. Figure 13 shows the  $\sigma_8$  constraints for varying  $l_{\max}$  values for the LSST/CMB-S4 measurement. We can see that  $l_{\max}$  can sig-

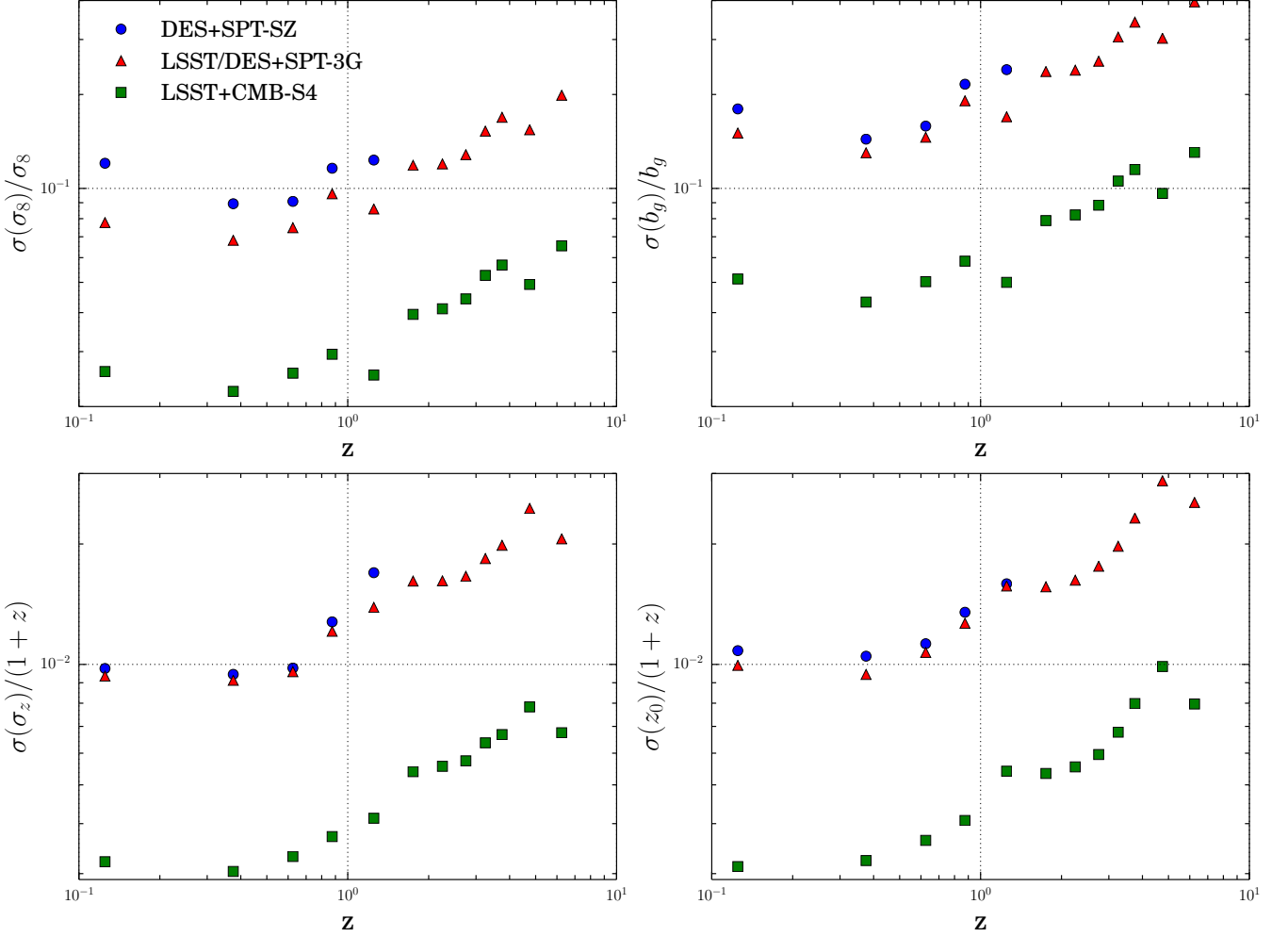


FIG. 11. The Constraints on all four of our redshift bin parameters,  $\sigma_8$ ,  $b_g$ ,  $z_0$  and  $\sigma_z$  for each of the survey combinations for our fiducial analysis including redshift uncertainties. Each of the surveys use  $l_{\max} = 1000$ . The correlations with SPT have  $f_{\text{sky}} = 0.061$  ( $2,500 \text{ deg}^2$ ) and the correlation of LSST and CMB-S4 has  $f_{\text{sky}} = 0.5$  ( $20,000 \text{ deg}^2$ ). The results for DES+SPT-3G and LSST+SPT-3G are within 5% of each other for the redshift bins DES goes up to, so only LSST+SPT-3G is plotted. In general constraints are better with higher densities and thus decrease with redshift, though there are exceptions where the bin size is increased in redshift width from the previous bin (e.g.,  $z = 1.25$ ). We plot here logarithmically on the x-axis to give more space in showing the DES constraints while still showing the full redshift range of LSST.

nificantly impact the constraints. Increasing  $l_{\max}$  from 1000 to 2000 approximately doubles the constraining power for the  $z < 1.5$  bins, though makes less of a difference in the higher redshift bins.

### C. Dependence on $f_{\text{sky}}$

Another important parameter to study is the overlapping sky fraction of the surveys,  $f_{\text{sky}}$ . We show our fiducial analysis of LSST/CMB-S4 for a range of  $f_{\text{sky}}$  values in Figure 14. The constraints on parameters scale as  $\sim 1/\sqrt{f_{\text{sky}}}$  due to the factor of  $f_{\text{sky}}$  in Equation 8. On the far left of the plot, is the value  $f_{\text{sky}} = 0.061$ , which is the overlap of DES and SPT. Keeping all other parameters the same, the increase from this overlap,

to our fiducial value of  $f_{\text{sky}} = 0.5$  with LSST and CMB-S4 increases constraints on  $\sigma_8$  by almost a factor of three. This highlights the importance of having maximal overlap between CMB-S4, which is still in the planning phases, and LSST. We also note that based on this scaling, a possibly more realistic value of  $f_{\text{sky}} = 0.45$  ( $18,000 \text{ deg}^2$ ) for LSST will degrade constraints by approximately 5% compared to the results in our fiducial analyses using  $f_{\text{sky}} = 0.5$ .

### D. Dependence on CMB Lensing noise

In this section, we study the how the  $\sigma_8$  constraints change when varying the CMB lensing noise alone. As shown in Figure 2, the three CMB experiments have different amounts of

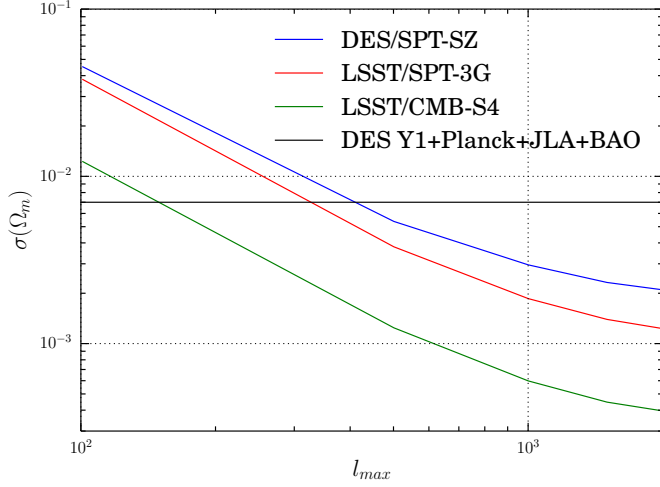


FIG. 12. The constraints on  $\Omega_m$  for each of the survey combinations for our fiducial analysis including redshift uncertainties (same analysis as Figure 11). As an example of current constraints on  $\Omega_m$  from photometric surveys, we show the constraint from the recent DES year 1 analysis [6] when combined with CMB data from Planck, Type Ia supernovae data from the Joint Light-curve Analysis (JLA) and BAO data from multiple surveys (see references in [6]).

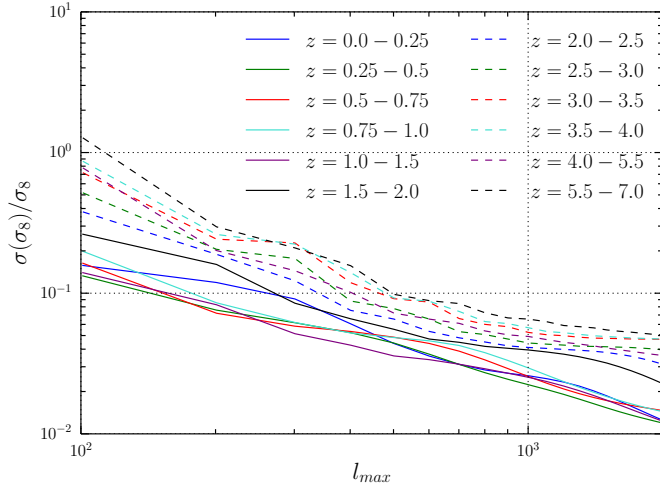


FIG. 13. Dependence on  $l_{max}$  for the  $\sigma_8$  constraints. We use the fiducial parameters of LSST and CMB-S4, including  $f_{sky} = 0.5$ .

CMB lensing noise. In Figure 15, we show the constraints on  $\sigma_8$  for LSST/CMB-S4 when varying the CMB lensing noise. We vary the lensing noise by multiplying the fiducial CMB-S4 noise curve (Figure 2) by a constant factor. SPT-SZ is approximately 50-100 times more noise than CMB-S4, and SPT-3G is about 3-8 times more noise than CMB-S4 for comparison, with the factor changing with  $l$ . We see overall in Figure 15 that constraints only modestly depend on lensing noise, at least in the LSST era of galaxy densities. We see that

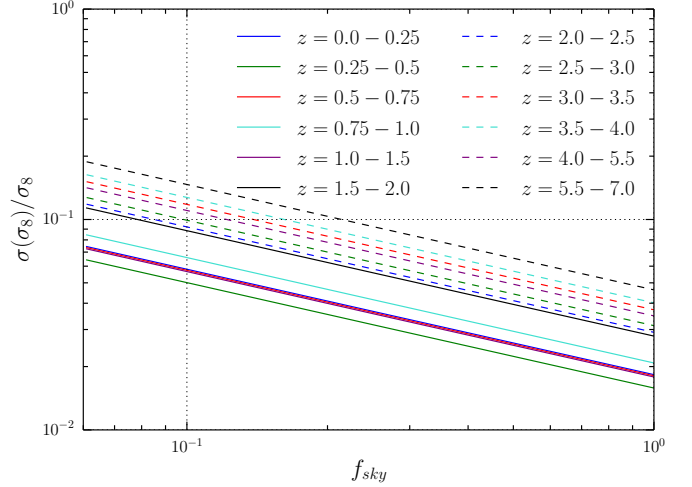


FIG. 14. Dependence on  $f_{sky}$  for the  $\sigma_8$  constraints. We use the fiducial parameters of LSST and CMB-S4, including  $l_{max} = 1000$ . The dependence scales as  $\sim 1/\sqrt{f_{sky}}$ .

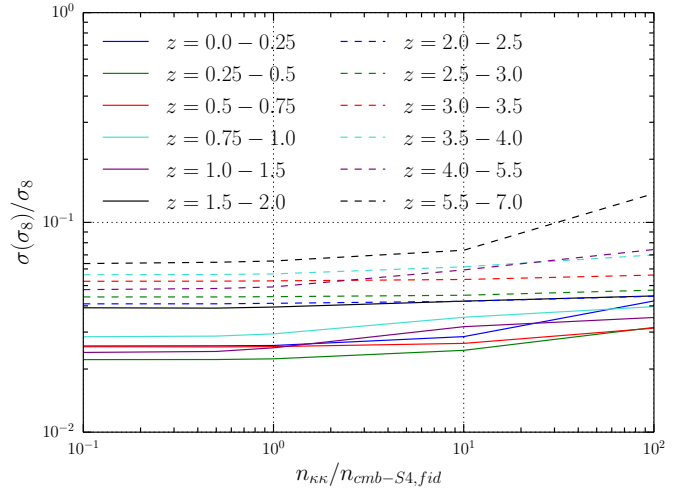


FIG. 15. Dependence of the  $\sigma_8$  constraints on CMB lensing noise in units of the fiducial prediction for CMB-S4 lensing noise. SPT-SZ is similar to a factor of about 50-100 times the lensing noise as CMB-S4. SPT-3G has about 3-8 times the noise of CMB-S4. All other parameters match the fiducial LSST+CMB-S4 analysis.

increases in constraining power become less significant as the noise is decreased to lower than the fiducial CMB-S4 noise curve.

### E. Dependence on Galaxy Density

In this section, we study how the constraints on  $\sigma_8$  depend on the galaxy density. In the bins that overlap, LSST should have about 3-5 times as many galaxies as DES. Figure 16

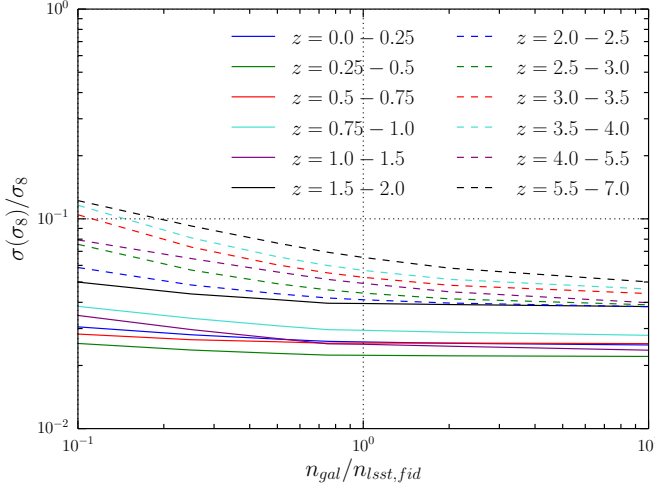


FIG. 16. Dependence of the  $\sigma_8$  constraints on galaxy density in units of fiducial LSST prediction. LSST has about 3-5 as many galaxies as DES in the bins that they overlap in. All other parameters match the fiducial LSST+CMB-S4 analysis.

shows how the fiducial LSST/CMB-S4 analysis changes when the overall galaxy density is changed. We vary the galaxy density at all redshifts by a constant factor. The figure shows only modest dependence on galaxy density. It also shows clearly that going from roughly the current era of a DES-like galaxy density to LSST produces a greater increase in precision than another factor of 3-5 would in higher galaxy density.

The results of Figures 15-16 show that in isolation, improving LSST and CMB-S4 noise only marginally improves cosmological analyses using cross-correlations of galaxies and CMB lensing. As also found in [19], these future surveys appear to be in somewhat of a sweet spot, where significant improvements could only be made by improving both the galaxy and CMB sides, and not one or the other.

## F. Dependence on Redshift Priors

So far, our analysis has assumed no priors on any of the cosmological or redshift parameters we vary. In this section, we see how our results change when adding priors on the redshift parameters. As mentioned, photometric surveys like DES and LSST put considerable effort into calibrating photometric redshift methods, so any real analysis will have some level of prior on quantities like  $z_0$  and  $\sigma_z$ . We apply a range of plausible priors for LSST redshifts to our analysis. The most recent LSST DESC Science Requirements Document [54] provides some targets for redshift priors on galaxy samples. In it, the precision on the mean redshift of photometric bins to be used in large-scale structure measurements (in the full 10-year analyses) is required to be  $0.003(1+z)$  in order to not significantly degrade cosmological measurements. Similarly, a precision of  $0.03(1+z)$  on the width of the redshift distribution is required for the same samples of galaxies. The

precision for samples of galaxies to be used as weak lensing sources are tighter,  $0.001(1+z)$  and  $0.003(1+z)$  for the mean and width of the redshift distributions respectively. For some redshift ranges, the priors on redshifts may be significantly better than these numbers for LSST. In [55], the spatial cross-correlation of photometric and spectroscopic galaxies could yield constraints on both the mean and width of redshift bins of  $\approx 0.0004(1+z)$  for  $z = 0.5 - 1.5$ . The exact priors available in the LSST era will depend on a number of factors, including the number, redshift range, and magnitude depth of spectroscopic samples, the number density of the photometric samples, the types of galaxies in the photometric samples and the width of the photometrically selected bins ( $\sigma_z$ ). Each of these factors can make constraints significantly weaker at higher redshifts.

We use the numbers mentioned in the previous paragraph as a broad range of possible priors available in the LSST era. In Figure 17, we plot how the constraints on  $\sigma_8(z)$  change for a range of prior assumptions on  $z_0$  and  $\sigma_z$ . We plot the different scenarios for both  $l_{\max} = 1000$  and 2000. We use the simple model of having just  $z_0$  priors, just  $\sigma_z$  priors, or priors on each of the same magnitude. We make the broad assumption of having the priors scale as  $(1+z)$ . We can see in Figure 17 that the priors on  $\sigma_z$  are more important than the priors on  $z_0$  for constraining  $\sigma_8$ . This makes sense, as  $\sigma_z$  and  $\sigma_8$  both provide an overall scaling to the galaxy auto-correlations, which have the highest S/N of any of the power spectra. Meanwhile the dependence on  $z_0$  is less degenerate with  $\sigma_8$ . (See Appendix A).

We can see in Figure 17 that redshift priors can improve the constraints on  $\sigma_8$  considerably. For the case of priors of  $0.003(1+z)$  on both  $z_0$  and  $\sigma_z$ , the constraints on  $\sigma_8$  improves by about a factor of 2-3 from the no priors case. When adding priors of  $0.0004(1+z)$ , the constraining power is within 50% of the no redshift uncertainty scenario ( $z_0$  and  $\sigma_z$  fixed). This model however is almost certainly too optimistic for  $z > 1.5$ . We also see that a prior of  $0.03(1+z)$  (the current LSST DESC requirement for  $\sigma_z$ ) adds nearly zero constraining power for our fiducial analysis of LSST/CMB-S4.

In Figure 18, we show a similar analysis for the DES+SPT-SZ era for  $l_{\max} = 1000$  and 2000. We project DES redshift parameter priors on the order of 0.01-0.02 based on recent calibrations of redshift bins in DES Year 1 cosmological analyses. The weak lensing source galaxies used in [6] and [8] are separated into photometrically-selected bins. The mean redshift of these bins are constrained to about an accuracy of 0.02 both in tests of photometric redshift methods on samples of spectroscopically measured galaxies [22] and in using spatial cross-correlations with spectroscopic galaxies [26]. These results were pretty constant across redshift, so we do not vary our priors with the factor  $(1+z)$  here. The brighter redMaGiC galaxies used in DES year 1 results ([56], [71]) had tighter constraints on their mean redshifts from cross-correlations with spectroscopic galaxies [25]. However, the modeled galaxy densities in our paper are much higher than this sample, making the weak lensing source sample a more appropriate sample to use for plausible redshift priors.

We overall see a similar dependence on redshift priors for

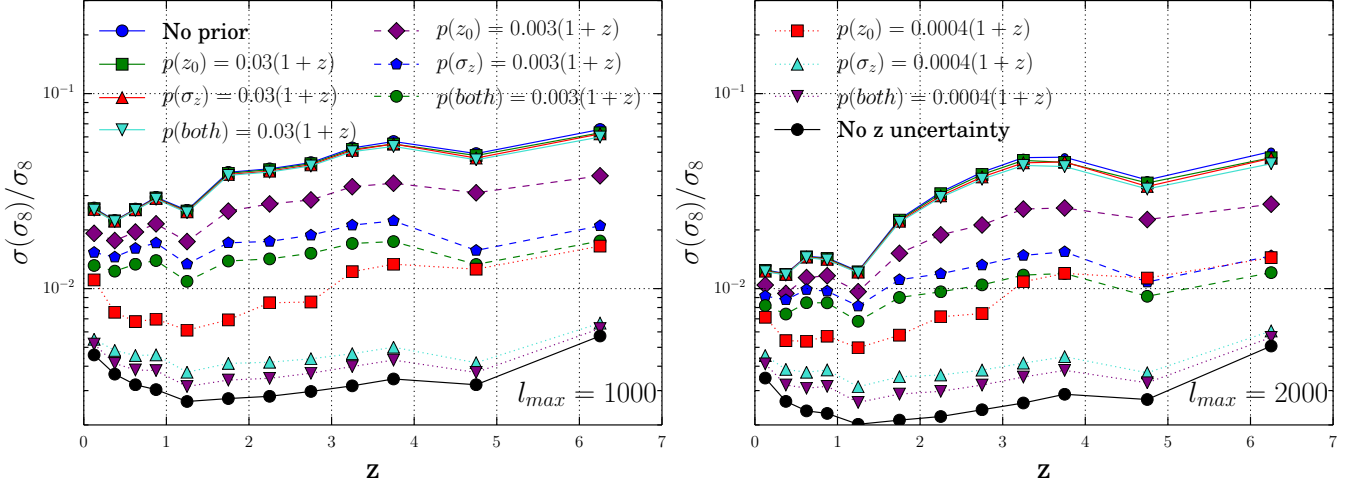


FIG. 17. Constraints on  $\sigma_8$  for our fiducial LSST/CMB-S4 analysis when adding priors on redshift parameters. Left: constraints when having  $l_{\max} = 1000$ . Right: constraints when having  $l_{\max} = 2000$ . Each curve adds either a prior on  $z_0$ , on  $\sigma_z$  or an equal prior on each. We compare the curves with priors to the fiducial case of no priors, and the opposite extreme of no redshift uncertainty with  $z_0$  and  $\sigma_z$  fixed in the Fisher analysis. The priors of  $0.003(1+z)$  and  $0.03(1+z)$  come from the LSST DESC SRD requirements ([54]) for  $z_0$  and  $\sigma_z$ , respectively. The prior of  $0.0004(1+z)$  is a plausible future achievement by clustering redshifts at low  $z$  found in [55].

the DES/SPT-SZ era as the future LSST/CMB-S4. Tightening the redshift priors brings results closer to the case of no redshift uncertainty. We again see that  $\sigma_z$  is more important than  $z_0$  for constraining  $\sigma_8$ . In the DES year 1 analysis ([6] and the others mentioned above), only  $z_0$  was constrained. Figure 18 (left) shows that adding a 0.02 prior on  $\sigma_z$  to the already achieved 0.02 prior on  $z_0$  would improve constraints on  $\sigma_8$  for the highest two redshift bins by about 30%. If  $l_{\max}$  can be extended to 2000 (right side of 18), the gains of a 0.02 prior on  $\sigma_z$  only go up to 15%.

### VIII. CONSTRAINTS ON REDSHIFT PARAMETERS

We focus briefly again in this section on the ability of galaxy clustering and galaxy-CMB lensing correlation measurements to ‘self-calibrate’ redshifts and compare those constraints to photometric redshift techniques. The idea of calibrating redshifts strictly from correlation functions was studied in more detail recently in [28]. A significant difference in this work though is not fixing the cosmology while solving for redshift parameters.

As mentioned in Section VII F, the Dark Energy Survey is already calibrating the mean redshift of bins to an uncertainty of about 0.02. The Large Synoptic Survey Telescope broadly has a requirement of constraining the mean of redshift bins to  $0.003(1+z)$ , though likely that number can be beaten at low redshifts as mentioned in Section VII F. In Figure 19, we compare the LSST DESC SRD [54] required redshift constraints, and the current DES redshift constraints to our Fisher analysis of  $\sigma_z$  and  $z_0$  with no priors applied. We show results for both  $l_{\max} = 1000$  and 2000 in Figure 19. The projections on DES from correlations with SPT beat the current threshold of 0.02

constraints on the redshift parameters in the first three redshift bins, even if only  $l_{\max} = 1000$  can be used. As mentioned previously, currently DES has only constrained the mean redshift of bins,  $z_0$  and not the width,  $\sigma_z$ . Work in e.g., [24] suggests constraints on each parameter should be comparable though from spatial cross-correlations with spectroscopic galaxies. For LSST, the constraints for  $l_{\max} = 2000$  at low redshifts ( $z < 1.5$ ) are stronger than the goal  $0.003(1+z)$  uncertainty on  $z_0$ . For  $l_{\max} = 1000$ , the constraints are weaker than this goal, though within a factor of 2 for  $z < 3$ . All of the constraints for both  $l_{\max}$  values are better than the LSST requirement on  $\sigma_z$  of  $0.03(1+z)$  for large-scale structure analyses. Even if the constraints of ‘self-calibrating’ redshifts from power spectra measurements are merely comparable to traditional methods of photometric redshift estimation, this could add significant information to cosmic surveys. A discrepancy could point to systematics in either the photometric redshift or power spectra measurements.

### IX. CONCLUSIONS

In this work, we sought to answer two questions: 1. How are analyses of galaxy clustering and CMB lensing affected by uncertainties in redshift parameters and 2. Can redshift parameters be self-calibrated by galaxy and CMB lensing correlations. We found in Section VI that the presence of redshift uncertainties can increase errors on e.g.,  $\sigma_8(z)$  by an order of magnitude. We showed the importance of using the cross-correlations of different galaxy bins ( $C_l^{g_i g_j}$ ), which in the assumption of perfect redshift knowledge is not a necessary measurement.

Though the redshift uncertainties degrade the analysis, the



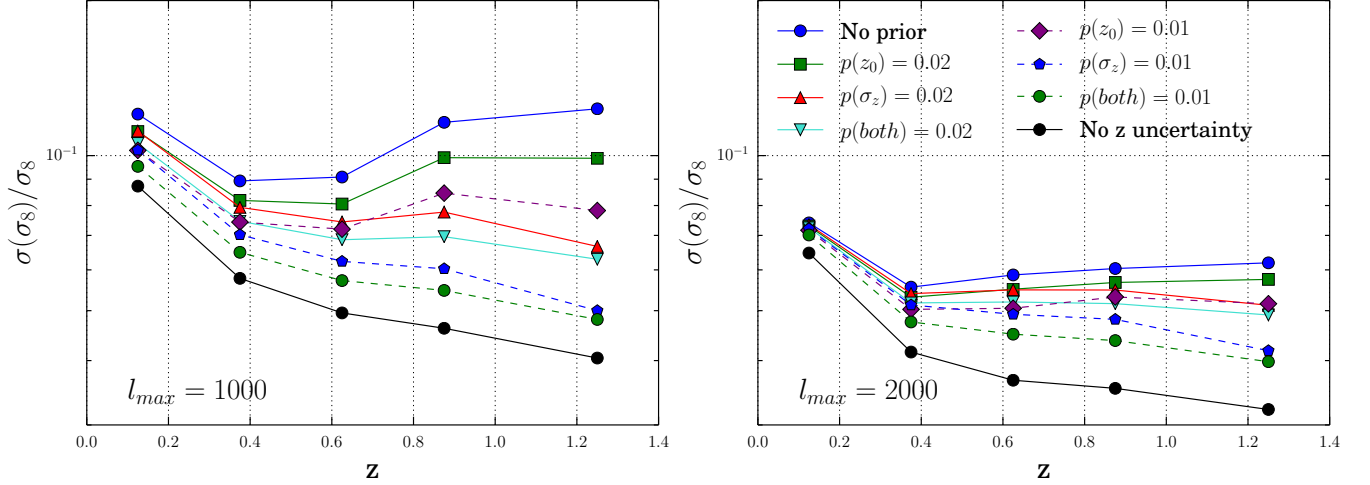


FIG. 18. Constraints on  $\sigma_8$  for the surveys DES/SPT-SZ with priors on the redshift parameters. Left: constraints with  $l_{\max} = 1000$ . Right: constraints with  $l_{\max} = 2000$ . We compare priors on  $z_0$ ,  $\sigma_z$  and both parameters with the case of no priors, and the case of no redshift uncertainty. We base the priors on recent DES results, and do not vary them with  $(1+z)$ , unlike Figure 17.

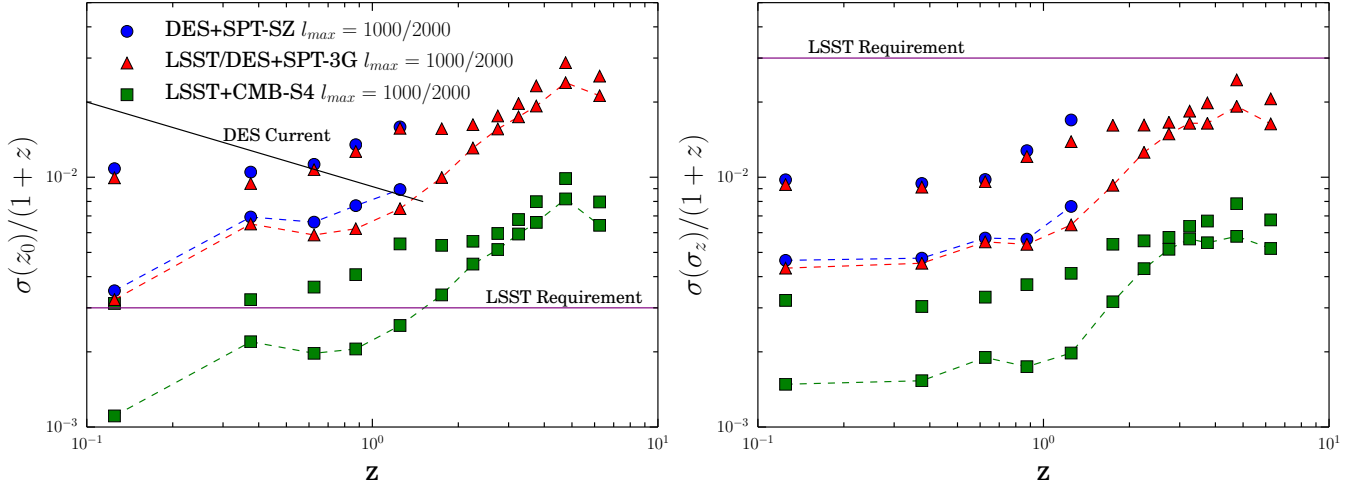


FIG. 19. The constraints on the mean of a binned redshift distribution (left) and the width of the distribution (right) for our fiducial analyses of different surveys. The unconnected points are with  $l_{\max} = 1000$  and the dotted lines are with  $l_{\max} = 2000$ . We compare these constraints to the current approximate DES constraints for mean redshifts in a bin from photometric redshift methods [26], and target constraints for both redshift parameters in LSST. The LSST requirements are from the LSST DESC Science Requirements Document [54]. We note that DES has not tried to constrain  $\sigma_z$  directly in data, so we only show a constraint on  $z_0$ . These constraints from DES are roughly constant with redshift, so we see a decrease with redshift when plotting  $\sigma(z_0)/(1+z)$ .

projected cosmological constraints are still fairly impressive. Our fiducial analysis (Figure 11) constrains  $\sigma_8$  in each redshift bin in the DES/SPT-SZ era to about 10%. For LSST/CMB-S4, the constraints get down to 2 – 3% at low redshifts ( $z < 1.5$ ), and only a few % higher at higher redshifts. Constraints of this level should help in distinguishing between e.g.,  $\Lambda$ CDM and models of modified general relativity as the cause of cosmic acceleration. As a comparison, [43] predicts 2% measurements on  $\sigma_8(z)$  from  $z = 0.5 - 3$  from LSST weak lensing and BAO data plus Planck CMB results, and finds that these

constraints could decisively rule out e.g., a DGP modified GR model [57].

In Section VII, we explored what survey parameters most affect these measurements of cosmological and redshift parameters. Among different survey parameters explored individually, we found the largest dependences on:  $f_{\text{sky}}$ ,  $l_{\max}$  and priors on the redshift parameters. The constraining power can be doubled or better by increasing  $l_{\max}$  from 1000 to 2000 (Figure 13) or with good priors on the redshift parameters from other data sources (e.g., Figure 17). The analysis of

$f_{\text{sky}}$  (Figure 14) shows that the significant increase in overlap of surveys in the future (LSST/CMB-S4 will have 8 times as much overlapping area as DES/SPT), accounts for much of the increased precision on  $\sigma_8$ . In contrast, we found that increasing the galaxy density (Figure 16) or reducing the CMB lensing noise (Figure 15) beyond expectations for LSST/CMB-S4 only marginally improve constraints. As also found in [19], the improvements of LSST and CMB-S4 in terms of galaxy density and CMB lensing noise seem to work together, such that improving either individually further has minimal gain.

We also showed in Section VIII the constraints on redshift parameters from the Fisher analysis and compared them to current and expected constraints on redshift parameters from photometric redshift techniques (Figure 19). The constraints projected in this work are comparable to the photometric techniques. This suggests that ‘self-calibration’ of redshift parameters from cosmological measurements themselves can be competitive with other techniques. That such constraints can be achieved simultaneously with cosmological constraints (i.e.  $\sigma_8$ ) is an important finding for the feasibility of this method as a redshift probe.

A number of assumptions were made in this work that may need more study in the future. The largest element that was a focus of this work was the redshift distribution modeling. A two-parameter Gaussian model may not be sufficient for accurately incorporating redshift distributions and their uncertainties into analyses on data. More work on the resilience of this model, and extensions to make the model more flexible should be done. An advantage of the simple model we use is the strong dependence of the power spectra on the redshift parameters. This allows for ‘self-calibration’ of redshift parameters from just the power spectra measurements. A risk in having too many redshift parameters is creating degeneracies where multiple redshift parameters may impact the power spectra in similar ways. Another effect we do not address is that of ‘catastrophic redshift errors’ (see e.g., [58]), where galaxies are placed into a photometric bin significantly offset from their true redshift. This is unlike our model of an unbiased Gaussian noise added to the redshift estimates in Section III. Adding such errors to our analysis would also significantly

add to the modeling parameter space. We leave such investigations for future work, though we note that [19] finds that these types of errors can be constrained from the galaxy clustering and galaxy-CMB lensing correlations, so their impact may be qualitatively different from the redshift-related degeneracies studied here. We also note that there may be inaccuracies in our analysis due to using the Limber approximation (Equation 7) at low- $l$ . This is discussed in Appendix B.

There are several other possibly impactful parameters not addressed in this work which are mentioned in [19], whose analysis we broadly followed in order to isolate the effects of adding redshift uncertainty. These factors include non-linear galaxy bias, non-Gaussian terms in the covariance, redshift space distortions, biases in the CMB lensing map, and differences between a Monte Carlo analysis and a Fisher analysis. [19] also notes that bispectra could add useful information to an analysis like this.

This work should highlight the importance of incorporating redshift uncertainty and modeling into cosmological analyses using galaxies and CMB lensing, as well as inspire more work on ‘self-calibrating’ redshifts with these and other measurements. While we did not use weak gravitational lensing of galaxies, similar concerns about redshift uncertainties and modeling should be studied for using that probe, and many of the techniques in this work could be applied. The issue of how to address redshift uncertainty has never been more important than the upcoming era of LSST, where we will be probing redshift regimes currently still sparse in available spectroscopic measurements for calibrating photometric redshift techniques.

## ACKNOWLEDGEMENTS

RC thanks Josh Frieman, Scott Dodelson, Sam Passaglia, Chihway Chang, Eric Baxter, Ami Choi, and Ben Hoyle for useful conversations related to this work. RC is supported by the Kavli Institute for Cosmological Physics at the University of Chicago through grant NSF PHY-1125897 and an endowment from the Kavli Foundation and its founder Fred Kavli.

- 
- [1] D. Huterer *et al.*, *Astroparticle Physics* **63**, 23 (2015), arXiv:1309.5385.
  - [2] B. Flaugher, *International Journal of Modern Physics A* **20**, 3121 (2005).
  - [3] J. T. A. de Jong *et al.*, *The Messenger* **154**, 44 (2013).
  - [4] C. Heymans *et al.*, *MNRAS* **427**, 146 (2012), arXiv:1210.0032.
  - [5] S. Miyazaki *et al.*, in *Ground-based and Airborne Instrumentation for Astronomy IV*, SPIE, Vol. 8446 (2012) p. 84460Z.
  - [6] T. M. C. Abbott *et al.* (Dark Energy Survey Collaboration), *Phys. Rev. D* **98**, 043526 (2018), arXiv:1708.01530.
  - [7] J. Elvin-Poole *et al.*, *Phys. Rev. D* **98**, 042006 (2018), arXiv:1708.01536.
  - [8] M. A. Troxel *et al.*, *Phys. Rev. D* **98**, 043528 (2018), arXiv:1708.01538.
  - [9] J. Prat *et al.*, *Phys. Rev. D* **98**, 042005 (2018), arXiv:1708.01537.
  - [10] T. M. C. Abbott *et al.* (Dark Energy Survey Collaboration), ArXiv e-prints (2018), arXiv:1801.03181 [astro-ph.IM].
  - [11] LSST Dark Energy Science Collaboration, ArXiv e-prints (2012), arXiv:1211.0310 [astro-ph.CO].
  - [12] Ž. Ivezić *et al.*, ArXiv e-prints (2008), arXiv:0805.2366.
  - [13] The Planck Collaboration, ArXiv Astrophysics e-prints (2006), astro-ph/0604069.
  - [14] K. M. Smith, O. Zahn, and O. Doré, *Phys. Rev. D* **76**, 043510 (2007), arXiv:0705.3980.
  - [15] T. Giannantonio *et al.*, *MNRAS* **456**, 3213 (2016), arXiv:1507.05551.
  - [16] J. A. Peacock and M. Bilicki, *MNRAS* **481**, 1133 (2018), arXiv:1805.11525.
  - [17] J. E. Carlstrom *et al.*, *PASP* **123**, 568 (2011), arXiv:0907.4445 [astro-ph.IM].

- [18] K. N. Abazajian *et al.*, *Astroparticle Physics* **63**, 66 (2015), arXiv:1309.5383.
- [19] M. Schmittfull and U. Seljak, *Phys. Rev. D* **97**, 123540 (2018), arXiv:1710.09465.
- [20] K. S. Dawson *et al.*, *A.J.* **145**, 10 (2013), arXiv:1208.0022 [astro-ph.CO].
- [21] M. Levi, C. Bebek, T. Beers, R. Blum, R. Cahn, D. Eisenstein, B. Flaugher, K. Honscheid, R. Kron, O. Lahav, P. McDonald, N. Roe, D. Schlegel, and representing the DESI collaboration, *ArXiv e-prints* (2013), arXiv:1308.0847 [astro-ph.CO].
- [22] B. Hoyle *et al.*, *MNRAS* **478**, 592 (2018), arXiv:1708.01532.
- [23] C. Bonnett *et al.*, *Phys. Rev. D* **94**, 042005 (2016), arXiv:1507.05909.
- [24] J. A. Newman, *Astrophys. J.* **684**, 88-101 (2008), arXiv:0805.1409.
- [25] R. Cawthon *et al.*, *MNRAS* (2018), 10.1093/mnras/sty2424, arXiv:1712.07298.
- [26] C. Davis *et al.*, *ArXiv e-prints* (2017), arXiv:1710.02517.
- [27] M. Gatti *et al.*, *MNRAS* **477**, 1664 (2018), arXiv:1709.00992.
- [28] B. Hoyle and M. M. Rau, *ArXiv e-prints* (2018), arXiv:1802.02581.
- [29] E. Baxter *et al.*, *MNRAS* **461**, 4099 (2016), arXiv:1602.07384.
- [30] D. Kirk *et al.*, *MNRAS* **459**, 21 (2016), arXiv:1512.04535.
- [31] A. Font-Ribera, P. McDonald, N. Mostek, B. A. Reid, H.-J. Seo, and A. Slosar, *JCAP* **5**, 023 (2014), arXiv:1308.4164.
- [32] A. Gorecki, A. Abate, R. Ansari, A. Barrau, S. Baumont, M. Moniez, and J.-S. Ricol, *A&A* **561**, A128 (2014), arXiv:1301.3010.
- [33] Y. Ono *et al.*, *PASJ* **70**, S10 (2018), arXiv:1704.06004.
- [34] C. C. Steidel and D. Hamilton, *A.J.* **104**, 941 (1992).
- [35] K. T. Story *et al.*, *Astrophys. J.* **779**, 86 (2013), arXiv:1210.7231.
- [36] A. van Engelen *et al.*, *Astrophys. J.* **756**, 142 (2012), arXiv:1202.0546.
- [37] Y. Omori *et al.*, *Astrophys. J.* **849**, 124 (2017), arXiv:1705.00743.
- [38] R. Adam *et al.* (Planck Collaboration), *A&A* **594**, A8 (2016), arXiv:1502.01587.
- [39] T. Okamoto and W. Hu, *Phys. Rev. D* **67**, 083002 (2003), astro-ph/0301031.
- [40] B. A. Benson *et al.*, in *Millimeter, Submillimeter, and Far-Infrared Detectors and Instrumentation for Astronomy VII*, SPIE, Vol. 9153 (2014) p. 91531P, arXiv:1407.2973 [astro-ph.IM].
- [41] J. E. Austermann *et al.*, in *Millimeter, Submillimeter, and Far-Infrared Detectors and Instrumentation for Astronomy VI*, SPIE, Vol. 8452 (2012) p. 84521E, arXiv:1210.4970 [astro-ph.IM].
- [42] K. N. Abazajian *et al.* (CMB-S4 Collaboration), *ArXiv e-prints* (2016), arXiv:1610.02743.
- [43] P. A. Abell *et al.* (LSST Science Collaboration), *ArXiv e-prints* (2009), arXiv:0912.0201 [astro-ph.IM].
- [44] L. E. Bleem *et al.*, *ApJ* **753**, L9 (2012), arXiv:1203.4808 [astro-ph.CO].
- [45] D. N. Limber, *Astrophys. J.* **117**, 134 (1953).
- [46] N. Kaiser, *Astrophys. J.* **388**, 272 (1992).
- [47] P. A. R. Ade *et al.* (Planck Collaboration), *A&A* **594**, A13 (2016), arXiv:1502.01587.
- [48] C. Howlett, A. Lewis, A. Hall, and A. Challinor, *JCAP* **4**, 027 (2012), arXiv:1201.3654 [astro-ph.CO].
- [49] A. Lewis, A. Challinor, and A. Lasenby, *Astrophys. J.* **538**, 473 (2000), astro-ph/9911177.
- [50] R. E. Smith, J. A. Peacock, A. Jenkins, S. D. M. White, C. S. Frenk, F. R. Pearce, P. A. Thomas, G. Efstathiou, and H. M. P. Couchman, *MNRAS* **341**, 1311 (2003), astro-ph/0207664.
- [51] E. J. Baxter *et al.*, *ArXiv e-prints* (2018), arXiv:1802.05257.
- [52] C. Modi, M. White, and Z. Vlah, *JCAP* **8**, 009 (2017), arXiv:1706.03173.
- [53] M. Crocce *et al.*, *MNRAS* **455**, 4301 (2016), arXiv:1507.05360.
- [54] R. Mandelbaum *et al.* (LSST Dark Energy Science Collaboration), *ArXiv e-prints* (2018), arXiv:1809.01669.
- [55] J. A. Newman *et al.*, *Astroparticle Physics* **63**, 81 (2015), arXiv:1309.5384.
- [56] E. Rozo *et al.*, *MNRAS* **461**, 1431 (2016), arXiv:1507.05460 [astro-ph.IM].
- [57] G. Dvali, G. Gabadadze, and M. Porrati, *Physics Letters B* **485**, 208 (2000), hep-th/0005016.
- [58] A. P. Hearin, A. R. Zentner, Z. Ma, and D. Huterer, *Astrophys. J.* **720**, 1351 (2010), arXiv:1002.3383.
- [59] D. Huterer, C. E. Cunha, and W. Fang, *MNRAS* **432**, 2945 (2013), arXiv:1211.1015.
- [60] M. Crocce, A. Cabré, and E. Gaztañaga, *MNRAS* **414**, 329 (2011), arXiv:1004.4640.

## Appendix A: Power Spectra Dependence on Parameters

To get a better intuition of which power spectra constrain which parameters, Figure 20 shows  $dC_l/d\theta$  for the various combinations of spectra and parameters for the redshift bins  $0.75 < z_{\text{ph}} < 1.0$  with  $z_0 = 0.871$  and  $\sigma_z = 0.117$  and the redshift bin  $2.0 < z_{\text{ph}} < 2.5$  with  $z_0 = 2.178$  and  $\sigma_z = 0.216$ . We show two redshift bins to broadly see trends of how dependence on different parameters changes with redshift.

We can see for the galaxy auto-power spectra (top row), which are also the highest S/N spectra, the parameters  $b_g$  and  $\sigma_8$  equivalently scale the spectra. We also see that increasing  $b_g$  and  $\sigma_z$  both directly scale the galaxy auto-power spectra at all scales (in our modeling of no scale-dependent galaxy bias). Other than a normalization factor of the step sizes in the plot, for the galaxy auto-spectra,  $b_g$ ,  $\sigma_8$  and  $\sigma_z$  are degenerate. Adding the galaxy-CMB lensing cross-spectra (middle row), can break the degeneracy of  $b_g$  and  $\sigma_8$ , but has little dependence on  $\sigma_z$ . The cross-spectra of adjacent galaxy redshift bins (bottom row) have a large dependence on  $\sigma_z$ , in a way that is not degenerate with other parameters. These plots show that both the galaxy-CMB lensing cross-spectra, and galaxy-galaxy cross-spectra are necessary to break the degeneracy between  $b_g$ ,  $\sigma_8$  and  $\sigma_z$  that arises in the galaxy auto-spectra when incorporating redshift uncertainties.

We can also see that the parameters  $z_0$  and  $\Omega_m$  are largely not degenerate with other parameters in the galaxy auto-spectra (top row). For this reason, constraints on these parameters are less correlated with e.g.,  $\sigma_8$  improvements (Figure 10).

## Appendix B: Impact of Low- $l$ limit

In this work, we use the Limber approximation (Equation 7) through out for computational speed. However, it is known that the approximation breaks down at large scales (low- $l$ , e.g., [59], [60]). [19] uses the Limber approximation for only

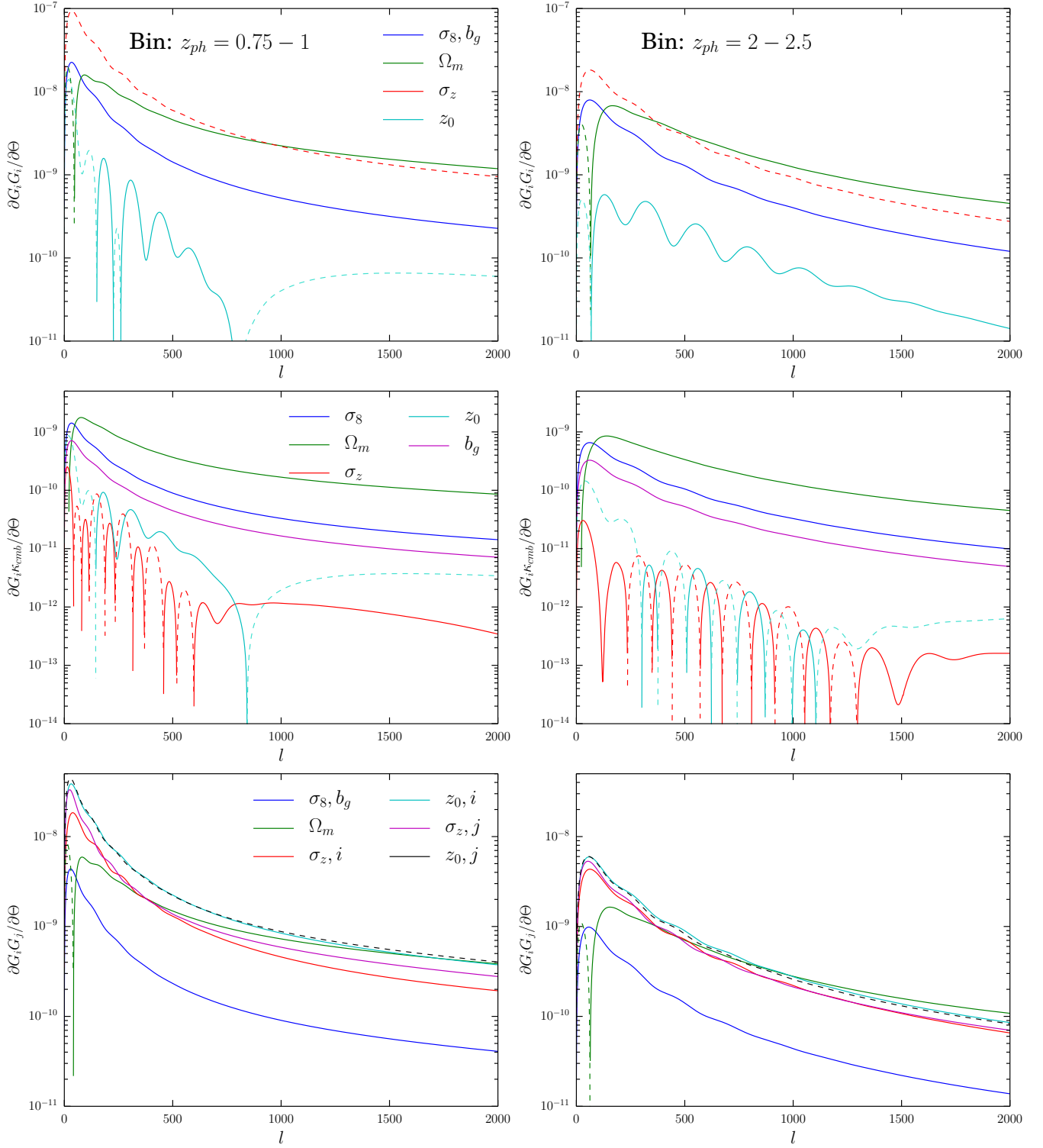


FIG. 20. Parameter dependence for the galaxy auto-power spectra (top), galaxy-CMB lensing cross spectra (middle row) and the cross spectra of two adjacent galaxy bins (bottom row). Shown are the spectra for the redshift bin  $0.75 < z_{ph} < 1.0$  (left) and  $2.0 < z_{ph} < 2.5$  (right). Dotted lines signify a negative correlation with the parameter and the spectra. For the galaxy cross spectra, the listed bins are the  $j$ th bin, and are cross-correlated with their neighboring lower redshift bins ( $0.5 < z < 0.75$  and  $1.5 < z < 2.0$  respectively) which are the  $i$ th bins in the bottom row.

$l > 50$ . We repeated our fiducial analysis (12 bins, 49 parameters, no priors, LSST/CMB-S4) using  $l_{\min} = 50$  instead of 20. We found that our constraints on all parameters for both the  $l_{\max} = 1000$  and 2000 cases degraded by 5% or less, with the exception of parameters in the three redshift bins separated by  $z = [0.75, 1, 1.5, 2]$  where much of the peak of the

power spectra is in the cut-out range of  $l = 20 - 50$ . In these bins, the constraints on  $\sigma_8$  degraded by [19%, 26%, 9%] and [7%, 14%, 3%] for the  $l_{\max} = 1000$  and 2000 cases respectively. These numbers are thus an upper limit to how much our results may degrade due to the likely inaccurate use of the Limber approximation at  $l = 20 - 50$ .